Pre-printed version of the paper published in the journal: International Journal for Numerical Methods in Engineering, Vol.96, pp150-175, 2013

An XFEM frame for plate elements in yield line analyses

Jin Xu, C.K. Lee, K.H. Tan

xu0003in@e.ntu.edu.sg

Summary

A high gradient zone (HGZ) comes into existence in both rotation and deflection displacement fields in the vicinity of a yield line in a plate structure with elasto-plastic material. This HGZ makes the displacements non-smooth locally around the yield line. The Extended Finite Element Method (XFEM) has been proved to be an effective numerical method to capture the behavior of a structure with a locally non-smooth displacement field. In this article, a 6-node triangular and a 9-node quadrilateral Mindlin-Reissner plate element with the XFEM formulation are presented to trace the elasto-plastic behavior of a plate in small-deformation analyses. Regularized enrichments are employed to enrich the rotation and the deflection displacement approximation fields simultaneously so that the non-smoothness in a displacement field near a yield line can be captured. The discrete shear gap method (DSG) is adopted to alleviate shear locking phenomena in the present XFEM plate element. Several plate bending examples are simulated to show the robustness of the enrichment in capture the high gradient zone resulted from yield lines and the effectiveness of the application of DSG method in controlling the shear locking in the XFEM plate element.

Key words: extended finite element method, plate element, the discrete shear gap method, high gradient zone, yield line, regularized enrichment

1 Introduction

A yield line results in a high gradient zone (HGZ) in both rotation and deflection displacement field in plate structures. In the HGZ, rapid changes in the rotational field and in the gradient of the deflection field occur within a short range normal to the yield line, as shown in Figure 1. The rapid changes make the displacement field non-smooth locally near the yield line. Different from a *real* discontinuity such as a crack in a plate, this non-smoothness is formed within a short range or a finite dimension. Therefore, this non-

smoothness due to a yield line is usually associated with the term 'high gradient' [1]. During the elasto-plastic analysis of a plate in a bending-dominant case, a point at the extreme layer of the plate yields first when the effective stress reaches the yield strength of the material. More material points in the plate reach yield with loading increases. The yielded zone extends to the middle layer in the thickness direction and spreads to the nearby area. A yield line forms when a continuous area has yielded and a plastic mechanism forms when sufficient yield lines coalesce together in the plate. After the plastic mechanism has formed, loading cannot be further increased and the plate structure may eventually collapse. During the above yielding and collapsing process, the non-smoothness resulted from the yield line comes into existence gradually as the load level increases.

In order to capture the behavior of a plate structure in an elasto-plastic analysis by using the standard finite element method (FEM), a locally fine mesh is required to be generated at the beginning of an analysis or a refinement of a coarse mesh pattern in the process of an analysis around the yield line is needed to be conducted. Hence, a large amount of computational effort is required. Compared to the FEM, the Extended Finite Element Method (XFEM) [2, 3] offers a great advantage to model non-smooth physical phenomena. In an XFEM analysis, special functions, which can describe the locally non-smooth displacement field based on *a priori* knowledge, are added into the displacement approximation fields. These special functions are called *enrichment functions*. Since the enrichment functions are selected to simulate the non-smooth displacement field, the XFEM makes it possible to capture the behavior of a plate structure in elasto-plastic analysis with a coarse mesh and it is unnecessary to refine the coarse mesh in the vicinity of the yield line during the analysis.

The XFEM is first proposed by Belytschko and Black [2] and Moës *et al.* [3] to model crack growth inside a plane element. A crack inside a plane element is regarded as a discontinuity with zero length. The Heaviside function, which generates a strong discontinuity in a displacement field, is added into the displacement approximation field as an enrichment to model the crack development. Sukumar *et al.* [4] introduced a level set function, which is discontinuous in a displacement gradient field, to model a weak discontinuity inside an element such as an interface of two materials. Zi and Belytschko [5] and Moës *et al*. [6] proposed shifted enrichments to the displacement field so that the enrichments are non-zero over the domain of interest, which is only a small portion of the whole physical domain. Patzák and Jirásek [7] proposed Regularized Heaviside function to model cohesive cracks and shear bands. Arias and Belytschko [8] adopted a tangent hyperbolic function, which

varies rapidly in one direction and slowly in the other, to model shear band growth. Benventi *et al.* [9, 10] adopted a regularized framework for discontinuity with a conspicuous finite length to model cohesive cracks. Inspired by the smoothed finite element method [11, 12], Bordas and his colleagues [13, 14] extended the strain smoothing technique [15] to XFEM. Vu-Bac [16] applied the node-based smoothed XFEM in fracture analyses. Chen et al [17] used the edge-based smoothed XFEM in linear elastic crack growth and Jiang et al [18] applied the edge-based smoothed XFEM in fracture analyses in composite materials. Up to now, many efforts have been done on engineering applications of the XFEM such as propagations of cracks [19-21], dislocations [22], interfaces of two different materials [4], two phase flow [23, 24], Burger's equation [25], solidification problems [26], biofilms [27, 28], swelling of hydrogels [29], yield analyses [30, 31]. In the meantime, extensive efforts have been devoted to simply to implementation of the XFEM, including to the numerical quadrature in XFEM formulation [3, 32-36] and stabilization of the stiffness matrix [37-40].

In [30], an XFEM formulation based on a 6-node triangular plate element is presented. In that element, the enrichment functions for high gradient zone are constructed by standard element shape functions. The enrichment functions are found to be sensitive to element shapes. Furthermore, the way to construct enrichment function by standard nodal shape functions is not applicable for 9-node quadrilateral elements, which is presented in Section 3 in this article. In this paper, a 9-node quadrilateral and a 6-node triangular C_0 plate element with the XFEM formulation to model the non-smooth displacement approximation fields near a yield line are presented. The aim of the present XFEM formulation is to capture the elasto-plastic behavior of a plate, with the help of *a priori* knowledge, by very few elements. The enrichments are constructed on structure level and they exhibit a high gradient normal to the yield line and a zero gradient along the yield line. The rotation and the deflection approximation fields are enriched simultaneously, with a regularized Heaviside function for rotation approximation field and a regularized level set function. The MITC technique [41] and the DSG technique [42] have been proved to be effective in both FEM and SFEM plate/shell analyses [43-48]. In this article, the discrete shear gap method (DSG) is employed to alleviate the shear locking in the XFEM plate elements. As the assumed shear strain field is interpolated by the nodal displacement variable, it is independent of the way a yield line cut across the enriched element.

In the next section, the governing equation for yield line analysis is presented. The enrichments for the rotation and the deflection displacements are introduced in Section 3. The

formulations of the XFEM plate element with DSG technique to alleviate shear locking are formulated in Section 4. In Section 5, the implementation of the XFEM formulation is introduced. Three examples are given in Section 6 to show the effectiveness of the enrichments proposed and the DSG method in the XFEM formulation, followed by conclusions and discussions in Section 7.

2 Problem statements

The detailed problem for yield line analyses can be described as follows: a plate structure domain Ω is bounded by Γ. The traction $\bar{\mathbf{t}}$ is defined on the boundary Γ_t and the displacement $\bar{\mathbf{u}}$ defined on the boundary Γ_u. The sub-domain Ω_{ns} denotes the high gradient zone resulted from a yield line. Given the spaces

$$\mathcal{U}_0 = \{\mathbf{u} \in C_0,\ \mathbf{u} = 0 \text{ on } \Gamma_u,\ \mathbf{u} \text{ is of high gradient within } \Omega_{ns}\} \tag{1}$$

and

$$\mathcal{U} = \{\mathbf{u} \in C_0,\ \mathbf{u} = \bar{\mathbf{u}} \text{ on } \Gamma_u,\ \mathbf{u} \text{ is of high gradient within } \Omega_{ns}\} \tag{2}$$

The equilibrium equation is solved by finding $u \in \mathcal{U}$,

$$\int_\Omega \boldsymbol{\varepsilon}(\mathbf{v})^{\mathrm{T}} \cdot \boldsymbol{\sigma}(\boldsymbol{\varepsilon}(\mathbf{u}))\mathrm{d}\Omega - \int_\Omega \mathbf{g} \cdot \mathbf{v}\mathrm{d}\Omega - \int_{\Gamma_t} \bar{\mathbf{t}} \cdot \mathbf{v}\mathrm{d}\Gamma = 0\,,\ \forall \mathbf{v} \in \mathcal{U}_0 \tag{3}$$

where $\boldsymbol{\sigma}$ is the Cauchy stress and $\mathbf{g}$ is the body force. Small strain assumption is employed and the strain $\boldsymbol{\varepsilon}$ is expressed as

$$\boldsymbol{\varepsilon} = \nabla_s \mathbf{u} \tag{4}$$

where ∇_s is the symmetric gradient operator. The constitutive relationship is

$$\boldsymbol{\sigma} = \mathbf{C}\boldsymbol{\varepsilon} \tag{5}$$

where $\mathbf{C}$ is the material matrix.

3 The enrichment functions

In a high gradient zone resulted from yield lines, both of the rotation and the deflection displacement field vary rapidly normal to the yield line. Meanwhile, in a C_0 Mindlin-Reissner plate element, rotation and deflection are interpolated independently. Therefore, the rotation and the deflection approximation field are enriched separately inside a HGZ. The enrichments for both rotation and deflection displacement field should at least be C_1 continuous over the whole physical domain. Furthermore, along the direction perpendicular to the yield line, the sign of the rotation and the deflection gradient should be opposite on the two sides of the yield line. On the other hand, the variation of rotation displacement and the gradient of deflection displacement along the yield line direction are smooth. Thus, the enrichments for both of the enriched displacement approximation field are cylinder-shape functions. It should be noted that the HGZ is an area with a high gradient in displacement fields and it should *not* be regarded as a yielded area. Meanwhile, in the present formulation, there is no additional technique to prevent a point outside a HGZ from yielding. The location and the width of a HGZ are regarded as *a priori* information.

3.1 Enrichment based on element level

The enrichment function presented in [49] is reviewed in this section. The enrichment function for deflection displacement is expressed as

$$F(\varphi)=\begin{cases} H & |\varphi|<0.5\omega \\ N_k|\varphi_k|-|N_k\varphi_k| & \text{otherwise} \end{cases} \tag{6}$$

where φ is the level set function, ω is the width of a high gradient zone, H is a Hermite function constructed within the high gradient zone and N_k is the standard shape function for node k in an enriched element. The enrichment is constructed at the element level and it vanishes to zero along the element edge unless the edge is cut by the non-smooth area. This enrichment function works well in a 6-node triangular element. However, it is found that it is not applicable for the 9-node XFEM plate element. The construction of this bubble-like enrichment function for the 9-node plate element is shown below to explain its failure in the 9-node plate element.

A particular case that $\varphi = r - s = 0$ and $\omega = 0.3$ of a high gradient zone in a quadrilateral element, as shown in Figure 3, is taken as an example. The plot of the enrichment function

for translational DOF in a 9-node quadrilateral element is shown in Figure 4. Two problems can be found from Figure 4. *First*, the enrichment function is not continuous at the interface between the high gradient zone and the smooth part. *Second*, the gradient of the enrichment function F along the yield line direction is not zero. The source of the first problem can be explained as follows: along the interface (η-direction in Figure 3), the function has three stationary points, which means that the highest order of η in the absolute level set function is 4. However, in the Hermite function, the order of η is up to 3. Therefore, the Hermite function is not able to reproduce the curve of the absolute level set function at their interface. Furthermore, it could be found that the fourth order term η^4 comes from the term r^2s^2 in the standard 9-node shape functions. The term r^2s^2 only appears in a 9-node plate element and disappears in an 8-node plate element. Therefore, by using an absolute level set function constructed by the standard shape function of an 8-node element, the problem of discontinuity at the interface could be solved. Hence, Equation (6) is modified as

$$F(\varphi)=\begin{cases} H & |\varphi|<0.5\omega \\ N_k|\varphi_k|-|N_k\varphi_k| & \text{otherwise} \end{cases},\quad k=1,2,...,8 \tag{7}$$

where N_k is the standard shape functions for an 8-node plate element. After the modification, the plot of the local enrichment function is shown in Figure 5 and it is found that the problem of the discontinuity at the interface of the high gradient zone and the smooth part is solved. However, the second problem still appears in the 9-node quadrilateral element.

3.2 Enrichment based on structural level

In order to implement the XFEM formulation in a 9-node quadrilateral element, an enrichment function which is independent of the standard nodal shape function is employed in this section. In the present XFEM plate element, a HGZ is defined on structure level by a level set function, $\varphi(X, Y) = 0$ and a width l_{ns}. An example of a HGZ with $\varphi = 0.8X - 0.6Y - 0.8 = 0$ and $l_{ns} = 1.5$ in a square domain $(X, Y) \in [0, 10] \times [0, 10]$ is shown in Figure 6.

The enrichment S for the rotation approximation field is expressed by

$$S_i(\varphi)=R(\varphi)-H(\varphi_i) \tag{8}$$

where $R(\varphi)$ is the regularized enrichment for the *rotation displacement* approximation field before shifting, which can be expressed as

$$R=\begin{cases}-1 & \varphi<-0.5l_{\mathrm{ns}}\\ \dfrac{3}{l_{\mathrm{ns}}}\varphi-\dfrac{4}{l_{\mathrm{ns}}{}^{3}}\varphi^{3} & -0.5l_{\mathrm{ns}}\le\varphi\le 0.5l_{\mathrm{ns}}\\ 1 & \varphi\ge 0.5l_{\mathrm{ns}}\end{cases} \tag{9}$$

$H(\varphi)$ is the Heaviside function, which is of the form:

$$H\left(\varphi\right)=\begin{cases}-1 & \varphi<0\\ 0 & \varphi=0\\ 1 & \varphi>0\end{cases} \tag{10}$$

$H(\varphi_i)$ (i = 1, 2, …, n_{node}) is the nodal value of the Heaviside function at node i. A plot of $S(\varphi)$ for the particular case is shown in Figure 7. Since the enrichment is shifted by Heaviside function, the problems due to blending elements are excluded in the rotation displacement approximation field [50].

The enrichment F for the *deflection displacement* approximation field used in the present formulation is of the form

$$F\left(\varphi\right)=\begin{cases}1.0-\dfrac{8}{l_{\mathrm{ns}}{}^{2}}\varphi^{2}+\dfrac{16}{l_{\mathrm{ns}}{}^{4}}\varphi^{4} & \left|\varphi\right|<0.5l_{\mathrm{ns}}\\ 0 & \text{otherwise}\end{cases} \tag{11}$$

A plot of $F(\varphi)$ for the particular example is shown in Figure 8. It could be seen that the $F(\varphi)$ is non-zero inside HGZ and zero outside HGZ. Hence PU condition is satisfied over the whole domain.

4 Formulations for the XFEM plate elements

4.1 The degrees of freedom and displacement approximation field

The plate element is initially flat and placed in 0xy plane. There are six DOFs per node in enriched elements, which is $\mathbf{u}_{\mathrm{enr}i}=(w_i,\theta_{\mathrm{x}i},\theta_{\mathrm{y}i},a_{\mathrm{x}i},a_{\mathrm{y}i},b_i)^{\mathrm{T}}$, ($i$ =1, 2, …, n_{node}). n_{node} is the total number of nodes in one element, for a 9-node element, n_{node} = 9, and n_{node} = 6 for a 6-node element. w_i is the out-of-plane deflection at node i and $\theta_{\mathrm{x}i}$ and $\theta_{\mathrm{y}i}$ are the rotational angle with

respect to x- and y-axis, respectively. The variables a_{xi} and a_{yi} are the additional rotational DOF with respective to the x- and y-axis whereas b_i is the additional translational DOF.

The deflection field w_h and rotation field θ_{xh} and θ_{yh} are approximated by the sum of the smooth part and the non-smooth part

$$w_h = w + b = N_i w_i + L_i b_i \tag{12}$$

$$\theta_{xh} = \theta_x + a_x = N_i \theta_{xi} + M_i a_{xi} \tag{13}$$

$$\theta_{yh} = \theta_y + a_y = N_i \theta_{yi} + M_i a_{yi} \tag{14}$$

where b, a_x and a_y are the non-smooth displacement approximation fields for deflection and rotations, L_i and M_i are the interpolation functions for the non-smooth translation and rotation displacement, respectively. In a small deformation analysis, the rotational DOF can be regarded as a vector as the translational DOF [51] so that Equation (13) and (14) are valid. L_i and M_i can be found by the multiplication of the non-smooth enrichment and window functions. In the present XFEM formulation, the standard shape functions are used as window functions for the localization of the enrichments

$$M_i = N_i S \tag{15}$$

$$L_i = N_i F \tag{16}$$

where S and F are enrichments for rotation and deflection displacement approximation field, respectively (Equation (8) and Equation (11)).

4.2 The kinematic equation and constitutive model

A layered model, as shown in Figure 10, is adopted in the present XFEM plate element so that the elasto-plastic behavior of a plate structure can be traced. The middle surface of an element is selected as the reference surface. The strain components, including the bending strain of the j^{th} layer $\boldsymbol{\varepsilon}_{bj}$ and the shear strain $\boldsymbol{\gamma}$, are expressed as:

$$\boldsymbol{\varepsilon}_{bj} = -z_j \boldsymbol{\chi} = -z_j \begin{pmatrix} \dfrac{\partial \beta_x}{\partial x} + \dfrac{\partial \alpha_x}{\partial x} \\ \dfrac{\partial \beta_y}{\partial y} + \dfrac{\partial \alpha_y}{\partial y} \\ \dfrac{\partial \beta_y}{\partial x} + \dfrac{\partial \alpha_y}{\partial x} + \dfrac{\partial \beta_x}{\partial y} + \dfrac{\partial \alpha_x}{\partial y} \end{pmatrix} \tag{17}$$

$$\boldsymbol{\gamma} = \begin{pmatrix} -\beta_{\mathrm{x}} - \alpha_{\mathrm{x}} + \dfrac{\partial w}{\partial x} + \dfrac{\partial b}{\partial x} \\ -\beta_{\mathrm{y}} - \alpha_{\mathrm{y}} + \dfrac{\partial w}{\partial y} + \dfrac{\partial b}{\partial y} \end{pmatrix} \tag{18}$$

where z_j is the distance between the reference surface and the middle surface of the j^{th} layer. $\boldsymbol{\chi}$ is the curvature, α_{x} and α_{y} are the rotation angles of the lines normal to the undeformed neutral surface in x-z and y-z plane, respectively, which can be written in matrix form as [52]

$$\begin{pmatrix} \beta_{\mathrm{x}} \\ \beta_{\mathrm{y}} \end{pmatrix} = \begin{bmatrix} 0 & -1 \\ 1 & 0 \end{bmatrix} \begin{pmatrix} \theta_{\mathrm{x}} \\ \theta_{\mathrm{y}} \end{pmatrix} \tag{19}$$

α_{x} and α_{y} are the rotation angles of the lines normal to the undeformed reference surface in x-z and y-z plane due to the non-smooth rotation:

$$\begin{pmatrix} \alpha_{\mathrm{x}} \\ \alpha_{\mathrm{y}} \end{pmatrix} = \begin{bmatrix} 0 & -1 \\ 1 & 0 \end{bmatrix} \begin{pmatrix} a_{\mathrm{x}} \\ a_{\mathrm{y}} \end{pmatrix} \tag{20}$$

In Equations (17) and (18), the partial derivative of the non-smooth displacement field is written as:

$$\frac{\partial \alpha}{\partial \boldsymbol{\xi}} = S \frac{\partial N_i}{\partial \boldsymbol{\xi}} \alpha_i + \frac{\partial S}{\partial \boldsymbol{\xi}} N_i \alpha_i \tag{21}$$

$$\frac{\partial b}{\partial \boldsymbol{\xi}} = F \frac{\partial N_i}{\partial \boldsymbol{\xi}} b_i + \frac{\partial F}{\partial \boldsymbol{\xi}} N_i b_i \tag{22}$$

where $\partial / \partial \boldsymbol{\xi} = (\partial / \partial \xi, \partial / \partial \eta)^{\mathrm{T}}$. Since the enrichments S and F are constructed on structure level, the first derivative of the enrichments with respect to the natural coordinate variables ξ and η can be obtained by the chain rule as follows

$$\frac{\partial S}{\partial \boldsymbol{\xi}} = \frac{\partial \mathbf{X}^{\mathrm{T}}}{\partial \boldsymbol{\xi}} \frac{\partial \varphi}{\partial \mathbf{X}} \frac{\partial R}{\partial \varphi} \tag{23}$$

$$\frac{\partial F}{\partial \boldsymbol{\xi}} = \frac{\partial \mathbf{X}^{\mathrm{T}}}{\partial \boldsymbol{\xi}} \frac{\partial \varphi}{\partial \mathbf{X}} \frac{\partial F}{\partial \varphi} \tag{24}$$

where $\partial \varphi / \partial \mathbf{X} = (a, b)^{\mathrm{T}}$. It is noted that the values of $\partial S / \partial \boldsymbol{\xi}$ and $\partial F / \partial \boldsymbol{\xi}$ depend on the values of the components in the matrix $\partial \mathbf{X}^{\mathrm{T}} / \partial \boldsymbol{\xi}$, which are related to the size of an enriched element in a mesh pattern. This could be a source of the dependence of the HGZ width (l_{ns}) on the

element size. The dependence of the width on mesh size is also reported in [53]. Hence, convergence cannot be achieved in the present formulation. However, as the purpose of the present study is to use few elements to capture the non-smooth displacement field resulted from a yield line, the enrichment function is only necessary when a coarse mesh is used. It should be noted that when a fine mesh is employed in an analysis, the FEM formulation is able to obtain an accurate prediction on the ultimate loading level without any enrichment.

In the present plate element, the out-of-plane stress components are not taken into account in the formulation [54]. The exclusion of the out-of-plane stress components is acceptable, since in bending-dominant cases, the transverse shear stresses are assumed as uniformly distributed along the thickness direction. However, as it is well known that the transverse stress is zero at the extreme fibers and maximum at the mid-surface which will be yielded at the very late stage, initial yielding is not affected by this omission. The plane-stress J_2 flow rule [55] is employed with the backward Euler algorithm [56] is employed in the present formulation.

4.3 The discrete shear gap method (DSG)

Shear locking is one of the major concerns in a compatible plate element formulation. The compatible shear strain field introduces parasitic shear energy into the element in pure bending cases when the thickness/length ratio is very small, and the plate element behaves much stiffer than expected for a thin plate. In the present element, the DSG method [42] is employed. One of the advantages of the application of the DSG method in the XFEM formulation is that the assumed shear strain field is interpolated by the nodal displacement variables instead of the compatible strain at some selected optimal strain points. This advantage shows a potential in the XFEM plate elements because in the XFEM formulations, a discontinuity or a HGZ could pass through an enriched element in several different possible ways. Therefore, an enriched element would *not* be partitioned by a HGZ in a unique way, as it is shown in Section 5.1, which makes it hard to determine the locations of optimal strain points. While by using the DSG method, the shear strain is constructed independent of the partition ways, and a unique assumed shear strain field could be obtained. Besides, the application of the DSG method in conventional plate and shell elements has shown that the DSG elements can pass bending patch tests and it is less sensitive to element distortion.

In the DSG method, a deflection is divided into two parts: the part due to pure bending and the part due to shear deformation. The deflection associated with shear deformation is expressed as

$$\Delta w_{\gamma} = \int_{x_0}^{x} \gamma \mathrm{d}x = w\big|_{x_0}^{x} - \int_{x_0}^{x} \beta \mathrm{d}x = w(x) - w(x_0) + \Delta w_{\mathrm{b}}(x) \tag{25}$$

where γ is shear strain, w is the total deflection, Δw_{b} is deflection due to pure bending and x_0 is the coordinate of a selected reference point in the element, at which the total deflection is assumed to be zero. The deflection due to shear deformation Δw_{γ} is the so-called shear gap and the shear gap at node i can be expressed as

$$\Delta w_{\gamma i} = w_i - w_0 + \Delta w_{\mathrm{b}i} \tag{26}$$

By discretization, the shear gap can be rewritten as

$$\Delta w_{\gamma} = N_i \Delta w_{\gamma i} \tag{27}$$

Thus the assumed shear strain can be obtained by the first derivative of shear gap field with respect to the coordinate

$$\tilde{\gamma} = \frac{\partial N_i}{\partial x} \Delta w_{\gamma i} \tag{28}$$

In the present XFEM plate element, the shear strain field is assumed as

$$\tilde{\gamma}_{\xi\zeta} = \frac{\partial \Delta w_{\xi\zeta}}{\partial \xi}, \quad \tilde{\gamma}_{\eta\zeta} = \frac{\partial \Delta w_{\eta\zeta}}{\partial \eta} \tag{29}$$

where $\Delta w_{\xi\zeta}$ is the shear gap obtained by integration of the compatible shear strain terms.

$$\Delta w_{\xi\zeta} = N_i \Delta w_{\xi\zeta i} = N_i \int_{\xi_1}^{\xi_i} \gamma_{\xi\zeta} \mathrm{d}\xi, \qquad \Delta w_{\eta\zeta} = N_i \Delta w_{\eta\zeta i} = N_i \int_{\eta_1}^{\eta_i} \gamma_{\eta\zeta} \mathrm{d}\eta \tag{30}$$

where $\gamma_{\xi\zeta}$ and $\gamma_{\eta\zeta}$ are compatible shear strain in curvilinear coordinate system.

Substituting Equation (30) into Equation (29) by using the kinematic equation for shear strain in Equation (18), the assumed shear strain can be expressed as

$$\gamma_{\xi\zeta} = -h_{\xi i} \beta_{\xi i} - h_{\xi i} S \alpha_{\xi i} + \frac{\partial N_i}{\partial \xi} w_i + \frac{\partial L_i}{\partial \xi} b_i \tag{31}$$

$$\gamma_{\eta\zeta} = -h_{\eta i}\beta_{\eta i} - h_{\eta i}S\alpha_{\eta i} + \frac{\partial N_i}{\partial \eta}w_i + \frac{\partial L_i}{\partial \eta}b_i \tag{32}$$

where $h_{\xi i}$ is the assumed shear strain interpolation function for the smooth rotation angle $\hat{a}_{\hat{i}}$ and the non-smooth rotation angle $S\alpha_{\xi}$ and $h_{\eta i}$ is the assumed shear strain interpolation function for the smooth rotation angle β_{η} and the non-smooth rotation angle $S\alpha_{\eta}$ in the curvilinear coordinate system.

The assumed shear strain in the global coordinate system can be obtained by

$$\begin{pmatrix} \gamma_{xz} \\ \gamma_{yz} \end{pmatrix} = \mathbf{S}^{-1} \begin{pmatrix} \gamma_{\xi\zeta} \\ \gamma_{\eta\zeta} \end{pmatrix} \tag{33}$$

where **S** is the orientation matrix at an integration point, which can be expressed as

$$\mathbf{S}^{\mathrm{T}} = \begin{bmatrix} \dfrac{\mathbf{e}_{\xi}}{|\mathbf{e}_{\xi}|} & \dfrac{\mathbf{e}_{\eta}}{|\mathbf{e}_{\eta}|} \end{bmatrix}, \quad \mathbf{e}_{\xi}{}^{\mathrm{T}} = \begin{pmatrix} \dfrac{\partial x_0}{\partial \xi} & \dfrac{\partial y_0}{\partial \xi} \end{pmatrix}, \quad \mathbf{e}_{\eta}{}^{\mathrm{T}} = \begin{pmatrix} \dfrac{\partial x_0}{\partial \eta} & \dfrac{\partial y_0}{\partial \eta} \end{pmatrix} \tag{34}$$

In Equation (34), x_0 and y_0 are x- and y-coordinates of the points on reference surface.

5 Implementation of the XFEM in the plate elements

5.1 Partition of an enriched element

In the present XFEM formulation, there are several possible ways of the partition of an enriched element. As shown in Figure 11 and Figure 12, an enriched element is divided into several geometries. In Figure 11 and Figure 12, 'TR' refers to triangular part, 'QU' refers to quadrilateral part, 'PE' refers to pentagon part, 'HE' refers to hexagon part, 'nH' refers to non-HGZ part (in blank) and 'H' refers to HGZ part (in shadow). When conducting numerical integration, a pentagon is divided into a triangular part and a quadrilateral part further, while a hexagon part is divided into two quadrilateral parts.

5.2 Numerical integration and the introduction of the XFEM formulation into analyses

Numerical integration is one of the major concerns in XFEM formulation. The numerical integration is conducted in each part by a 6 × 6 Gaussian integration scheme, which is sufficient to guarantee the non-singularity of the stiffness matrix of an enriched element, even

if the whole element domain is occupied by a HGZ (Figure 11c and Figure 12d). An enriched element is partitioned at the beginning of an analysis. Thus it is unnecessary to employ any additional criteria to check when to introduce the XFEM formulation during an analysis. Furthermore, no interpolation or extrapolation of stress and strain variables is needed. Therefore no additional error is brought into the XFEM analysis.

It is proved in [2] that introducing an enrichment with a jump into the FEM formulation is equivalent to adding a natural boundary condition to the corresponding enriched degree of freedom. However, different from a 'real' discontinuous enrichment, the introducing of a regularized enrichment is equivalent to expand the Ritz spaces of the numerical solution. Thus, although the regularized enrichments are added into the plate formulation before an analysis starts, the additional DOFs are suppressed automatically by the equilibrium condition in elastic stage and they will function only when they are needed in elasto-plastic stage and this stimulation of the regularized enrichment is also by the equilibrium condition automatically.

5.3 Scaled condition number

Ill-condition of the stiffness matrix is one of the major concerns in XFEM\GFEM formulation. In the present formulation, PARDISO solver [57] is employed, in which a preconditioning approach is used. The embedded preconditioning approach is based on maximum weighted matching and algebraic multilevel incomplete $\mathbf{LDL}^{\mathrm{T}}$ factorizations. In the numerical examples shown in Section 6, the scaled condition number k [39] of the initial stiffness matrices of the XFEM formulation and the FEM formulation with coarse mesh are listed. The scaled condition number is defined as

$$k = \frac{\lambda_{\max}(\mathbf{K})}{\lambda_{\min}(\mathbf{K})} \tag{35}$$

where $\lambda_{\max}(\mathbf{K})$ and $\lambda_{\min}(\mathbf{K})$ are the maximum and the minimum eigenvalue of the stiffness matrix $\mathbf{K}$, respectively. The scaled condition number becomes worse, when the ratio ρ is small [40]. The ratio ρ_i is defined as

$$\rho_i = \frac{A_i^*}{A_i} \tag{36}$$

where A_i* is the area of the portion of the node i support, where the enrichment is nonzero, A is the area of the whole support of node i, and node i is an enriched node.

6 Numerical examples

In this section, three examples are shown to illustrate the effectiveness of the XFEM formulation in capture the non-smoothness resulted from yield line and the DSG technique in control shear locking in XFEM elements. The computational costs, including the total number of DOF (n_{DOF}), Gaussian points (n_{GP}), stiffness matrix updating (n_s) and the CPU time (t_{CPU}), are listed in each example together with the scaled condition number of the stiffness matrices of the XFEM formulation and the FEM formulation with coarse mesh.

6.1 Example 1: A flat strip with two fully fixed ends

A flat rectangular plate is tested in this example, as shown in Figure 13. The length of the plate is L = 5.0 and the width is b = 1.0. The plate is fully fixed on the two short edges and free on the two long edges. The Young's modulus is $E = 1 \times 10^6$, while the Poisson's ratio is υ = 0.0. The mesh scheme of the uniform mesh patterns and the location of the three possible HGZ are shown in Figure 14. As the layered model is used in the present XFEM formulation, 5 layers are used for each element in this example.

6.1.1 Study on shear locking

In this section, shear locking is studied in the present XFEM formulation. Five cases with different thickness of the plate are tested. The yield strength and the reference loading are scaled according to the thickness (as listed in Table 1) so that the theoretical ultimate loading factors from yield line pattern analysis for the five cases are the same (λ_u = 0.625). The uniform mesh pattern is used in this study. The result from the present 6-node DSG XFEM plate element is shown in Figure 15, while the result from the 9-node DSG XFEM plate element is shown in Figure 16. Both of the results are compared with the corresponding conventional FEM analysis with the coarse mesh, as shown in Figure 14, a fine mesh (10 ×

50 × 2 for 6-node elements and 10 × 50 for 9-node elements) and the result from yield line pattern analysis [58] ($\lambda_u = 0.625$).

6.1.2 Comparison on the computational cost and the scaled condition number of the stiffness matrix

The computational costs, including the total number of DOF, Gaussian points, stiffness matrix updating and the CPU time, are listed in Table 2. The initial loading factor is taken as $\lambda_0 = 0.3$ for all the analyses. The analyses stops when the deflection w_A= -0.001m. It can be seen from Table 2 that all the three XFEM formulations can save a large amount of computational costs.

The condition number of the initial stiffness matrices of the XFEM formulation and the coarse mesh are also listed in Table 2. It can be seen that the condition numbers of the XFEM stiffness matrices are 2 or 3 orders higher than those of the FEM stiffness matrices with the same mesh.

6.1.3 Study on distorted mesh

In this section, a distorted mesh, as shown in Figure 17, is used to test the robustness of the enrichment. The term 'distorted' refers to angular distortion [59] without curved edge or shift of the mid-node. The geometrical and material properties of T1 case in Section 6.1.1 are used. The result from the 6-node XFEM plate element is shown in Figure 18 and the result from the 9-node XFEM plate element is shown in Figure 19.

6.2 Example 2: An L-shaped plate with two fully fixed ends

An L-shaped flat plate is tested in this example, as shown in Figure 20. Four cases with different thickness are tested to show the effectiveness of the DSG method applied in the XFEM formulation. The plate is fully fixed on the two short edges. The geometrical property is shown in Figure 20. The Young's modulus is $E = 1.0 \times 10^6$, while the Poisson's ratio is $\upsilon = 0.3$. The yield strength and the reference load vary according to thickness as listed in Table 3, so that the ultimate loadings for the four cases are the same. The mesh scheme and the

locations of three possible HGZs are shown in Figure 21. The width of the HGZs in this example is chosen as (l_{ns1}= l_{ns2} = 0.1, l_{ns3} = 1.0). As a layered model is employed in the present formulation, 5 layers are used for each element. The deflection of the corner point (point A in Figure 20) is investigated.

The results from the 6-node DSG XFEM plate elements and the 9-node DSG XFEM plate elements are shown in Figure 22 and Figure 23, respectively, with the results from the corresponding conventional plate elements by the coarse mesh (Figure 21), the result from the commercial software ANSYS and the yield line pattern analysis [58]. In the fine mesh analysis with 6-node plate element (in Figure 22), 1000 elements are used. In the ANSYS analysis, a total of 800 SHELL93 elements [60] with 5 layers for each element are employed. The yield line pattern analysis provides an upper bound solution, which is λ_u = 2.652.

The comparison on the computational costs and the scaled condition number of the initial stiffness matrices is listed in Table 4. It can be found that the XFEM formulation is able to save much computational costs while provides almost the same ultimate loading level, compared with the FEM formulation with a fine mesh.

The scaled condition number of the XFEM formulation is higher than that of the FEM formulation. Furthermore, the scaled condition number of the 9-node XFEM formulation is much worse than that of the 6-node XFEM formulation. This is because the ratios ρ_9, ρ_{11} and ρ_{12} (Equation (36)) (Figure 21b) in the 9-node XFEM formulation is only a half of that (Figure 21a) in the 6-node XFEM formulation.

6.3 Example 3: A square plate with roller supports at the four edges

A square plate supported by rollers on the four edges is tested in this example, as shown in Figure 24. The length of edge is 32. The Young's modulus is $E = 1.0 \times 10^{10}$, while the Poisson's ratio is υ = 0.2. A uniformly distributed loading is applied on the plate with the reference loading q_0. As listed in Table 5, four cases with different thickness are tested in this example. The yield strength and the reference loading vary according to the thickness so that the ultimate loading factors are the same for the four cases (λ_0 = 0.0586). A total of 5 layers are used in each element for the analyses. A quarter of the entire plate is modelled because of the symmetry condition. The yield line is along the diagonal line of the plate. The deflection

of the centre point (point A in Figure 24) is investigated. In this example, the HGZ width is assumed as $l_{ns} = 8$.

The results from the 6-node DSG XFEM plate elements and the 9-node DSG XFEM plate elements are shown in Figure 25 and Figure 26, respectively, comparing with the result from the FEM coarse mesh (as it is shown in Figure 24), yield line pattern analysis [58] and the result from the commercial software ANSYS. In the ANSYS analysis, a total of 400 SHELL93 elements [60] are employed. It is found that the variation of the thickness affects the ultimate loading level predicted by the present 6-node XFEM elements, while its influence is insignificant for the 9-node XFEM elements. This means that for this particular case, the shear locking is not controlled very well in the 6-node XFEM elements. However, the DSG technique is able to alleviate shear locking in the 9-node XFEM elements.

The comparison of the computational costs is listed in Table 6, together with the scaled condition number. Again, the XFEM formulation shows its advantage over the FEM formulation in reducing computational costs. The same phenomenon on the scaled condition number as that in Example 2 can be seen in this example: k is much greater in 9-node XFEM formulation than that in 6-node XFEM formulation. In this example, as shown in Figure 24 the ratios ρ_3, ρ_7, ρ_{11}, ρ_{15}, ρ_{19} and ρ_{23} in the 9-node XFEM formulation is a half of those in the 6-node XFEM formulation.

In order to investigate the influence of the mesh pattern on the XFEM formulation, an alternative mesh scheme, as shown in Figure 27 is employed. The Case T1 (Table 5) is chosen for the geometric and material property of the plate. The result is shown in Figure 28, together with the results from mesh pattern 1 for both FEM coarse mesh and XFEM (Figure 24a) and the yield line analysis [58]. It can be seen that the XFEM with the alternative mesh pattern improves the prediction on the ultimate loading level compared with the FEM analysis with the same mesh pattern. Besides, the prediction from the XFEM with mesh pattern 1 is closer to the result from yield line analysis than that from mesh pattern 1. This improvement also exists in FEM analysis. Hence, this sensitivity is not due to the enrichment in the XFEM formulation only.

7 Conclusions

An XFEM formulation for plate elements to capture a high gradient in displacement fields resulted from yield lines is presented. Regularized enrichments, which are C_1 continuous, are used for both rotation and deflection displacement approximation fields. The enrichments are constructed on structure level so that they are independent of the physical shape of an enriched element. The enrichments employed in the present formulation is non-zero inside a HGZ, so that the enrichment is confined within enriched elements only and several advantages can be seen: first partition of unity condition can be satisfied without additional technique; secondly, the Kronecker-δ condition can be satisfied so that the boundary condition can be applied easily; finally there is no unwanted strain terms in blending elements. The XFEM formulation is easy to be implemented in both triangular and quadrilateral plate elements and it is not sensitive to distorted mesh. As the enrichments are constructed by polynomials, the accuracy of the numerical integration on total potential energy could be controlled by Gaussian integration scheme precisely. The discrete shear gap method is adopted to control shear locking in both smooth and non-smooth shear strain field. Comparing with some other assumed strain methods, a set of assumed interpolation functions, which are associated with element nodes, are used to construct shear strain field in the DSG method. Thus it is feasible to apply this method in the XFEM formulation, in which an enriched element is partitioned into several parts. It is shown in the numerical examples that this method can control shear locking effectively in enriched elements.

However the width of HGZ is dependent on mesh size. A refined mesh could not provide a more accurate ultimate loading level with a fixed width of HGZ, which means the convergence could not be achieved. Besides the dependence of the HGZ width on mesh size, it is premature to state that the enrichment presented in this article is the best choice for the HGZ resulted from yield lines. Since the shape and the area of a HGZ depends on a few factors such as boundary condition and loading condition, a further study on choosing smarter enrichments independent of mesh size could be a research topic in future.

Reference

[1] Fries, T.-P. and T. Belytschko. The extended/generalized finite element method: An overview of the method and its applications. *International Journal for Numerical Methods in Engineering* 2010; **84(3)**: 253-304.

[2] Belytschko, T. and T. Black. Elastic crack growth in finite elements with minimal remeshing. *International Journal for Numerical Methods in Engineering* 1999; **45(5)**: 601-620.

[3] Moës, N., J. Dolbow and T. Belytschko. A finite element method for crack growth without remeshing. *International Journal for Numerical Methods in Engineering* 1999; **46(1)**: 131-150.

[4] Sukumar, N., D.L. Chopp, N. Moës and T. Belytschko. Modeling holes and inclusions by level sets in the extended finite-element method. *Computer Methods in Applied Mechanics and Engineering* 2001; **190(46-47)**: 6183-6200.

[5] Zi, G. and T. Belytschko. New crack-tip elements for XFEM and applications to cohesive cracks. *International Journal for Numerical Methods in Engineering* 2003; **57(15)**: 2221-2240.

[6] Moës, N., M. Cloirec, P. Cartraud and J.F. Remacle. A computational approach to handle complex microstructure geometries. *Computer Methods in Applied Mechanics and Engineering* 2003; **192(28-30)**: 3163-3177.

[7] Patzák, B. and M. Jirásek. Process zone resolution by extended finite elements. *Engineering Fracture Mechanics* 2003; **70(7–8)**: 957-977.

[8] Areias, P.M.A. and T. Belytschko. Two-scale shear band evolution by local partition of unity. *International Journal for Numerical Methods in Engineering* 2006; **66(5)**: 878-910.

[9] Benvenuti, E., A. Tralli and G. Ventura. A regularized XFEM model for the transition from continuous to discontinuous displacements. *International Journal for Numerical Methods in Engineering* 2008; **74(6)**: 911-944.

[10] Benvenuti, E. A regularized XFEM framework for embedded cohesive interfaces. *Computer Methods in Applied Mechanics and Engineering* 2008; **197(49-50)**: 4367-4378.

[11] Liu, G.R., K.Y. Dai and T.T. Nguyen. A Smoothed Finite Element Method for Mechanics Problems. *Computational Mechanics* 2007; **39(6)**: 859-877.

[12] Le, C.V., H. Nguyen-Xuan, H. Askes, S.P.A. Bordas, T. Rabczuk and H. Nguyen-Vinh. A cell-based smoothed finite element method for kinematic limit analysis. *International Journal for Numerical Methods in Engineering* 2010; **83(12)**: 1651-1674.

[13] Bordas, S.P.A., T. Rabczuk, N.-X. Hung, V.P. Nguyen, S. Natarajan, T. Bog, D.M. Quan and N.V. Hiep. Strain smoothing in FEM and XFEM. *Computers & Structures* 2010; **88(23–24)**: 1419-1443.

[14] Bordas, S.P.A., S. Natarajan, P. Kerfriden, C.E. Augarde, D.R. Mahapatra, T. Rabczuk and S. Dal Pont. On the performance of strain smoothing for quadratic and enriched finite element approximations (XFEM/GFEM/PUFEM). *International Journal for Numerical Methods in Engineering* 2011; **86(4-5)**: 637-666.

[15] Chen, J.-S., C.-T. Wu, S. Yoon and Y. You. A stabilized conforming nodal integration for Galerkin mesh-free methods. *International Journal for Numerical Methods in Engineering* 2001; **50(2)**: 435-466.

[16] Vu-Bac, N., H. Nguyen-Xuan, L. Chen, S. Bordas, P. Kerfriden, R.N. Simpson, G.R. Liu and T. Rabczuk. A Node-Based Smoothed eXtended Finite Element Method (NS-XFEM) for Fracture Analysis. *Cmes-Computer Modeling in Engineering & Sciences* 2011; **73(4)**: 331-355.

[17] Chen, L., T. Rabczuk, S.P.A. Bordas, G.R. Liu, K.Y. Zeng and P. Kerfriden. Extended finite element method with edge-based strain smoothing (ESm-XFEM) for linear elastic crack growth. *Computer Methods in Applied Mechanics and Engineering* 2012; **209**: 250-265.

[18] Jiang, Y., T.E. Tay, L. Chen and X.S. Sun. An edge-based smoothed XFEM for fracture in composite materials. *International Journal of Fracture* 2013; **179(1-2)**: 179-199.
[19] Areias, P.M.A. and T. Belytschko. Non-linear analysis of shells with arbitrary evolving cracks using XFEM. *International Journal for Numerical Methods in Engineering* 2005; **62(3)**: 384-415.
[20] Areias, P.M.A. and T. Belytschko. Analysis of three-dimensional crack initiation and propagation using the extended finite element method. *International Journal for Numerical Methods in Engineering* 2005; **63(5)**: 760-788.
[21] Stazi, F.L., E. Budyn, J. Chessa and T. Belytschko. An extended finite element method with higher-order elements for curved cracks. *Computational Mechanics* 2003; **31(1)**: 38-48.
[22] Belytschko, T. and R. Gracie. On XFEM applications to dislocations and interfaces. *International Journal of Plasticity* 2007; **23(10-11)**: 1721-1738.
[23] Chessa, J. and T. Belytschko. An enriched finite element method and level sets for axisymmetric two-phase flow with surface tension. *International Journal for Numerical Methods in Engineering* 2003; **58(13)**: 2041-2064.
[24] Jack Chessa and T. Belytschko. An Extended Finite Element Method for Two-Phase Fluids. *Journal of Applied Mechanics* 2003; **70(1)**: 10-17.
[25] Chessa, J. and T. Belytschko. Arbitrary discontinuities in space–time finite elements by level sets and X-FEM. *International Journal for Numerical Methods in Engineering* 2004; **61(15)**: 2595-2614.
[26] Chessa, J., P. Smolinski and T. Belytschko. The extended finite element method (XFEM) for solidification problems. *International Journal for Numerical Methods in Engineering* 2002; **53(8)**: 1959-1977.
[27] Duddu, R., S. Bordas, D. Chopp and B. Moran. A combined extended finite element and level set method for biofilm growth. *International Journal for Numerical Methods in Engineering* 2008; **74(5)**: 848-870.
[28] Bryan G. Smith, B.L.V. Jr. and D.L. Chopp. The extended finite element method for boundary layer problems in biofilm growth. *Communications in Applied Mathematics and Computational Science* 2007; **2(1)**: 35–56.
[29] Ji, H., H. Mourad, E. Fried and J. Dolbow. Kinetics of thermally induced swelling of hydrogels. *International Journal of Solids and Structures* 2006; **43(7–8)**: 1878-1907.
[30] Xu, J., C.K. Lee and K.H. Tan. A two-dimensional co-rotational Timoshenko beam element with XFEM formulation. *Computational Mechanics* 2012; **49(5)**: 667-683.
[31] Xu, J., C.K. Lee and K.H. Tan. An XFEM plate element for high gradient zones resulted from yield lines. *International Journal for Numerical Methods in Engineering* in press.
[32] Laborde, P., J. Pommier, Y. Renard and M. Salaün. High-order extended finite element method for cracked domains. *International Journal for Numerical Methods in Engineering* 2005; **64(3)**: 354-381.
[33] Ventura, G. On the elimination of quadrature subcells for discontinuous functions in the eXtended Finite-Element Method. *International Journal for Numerical Methods in Engineering* 2006; **66(5)**: 761-795.
[34] Ventura, G., R. Gracie and T. Belytschko. Fast integration and weight function blending in the extended finite element method. *International Journal for Numerical Methods in Engineering* 2009; **77(1)**: 1-29.
[35] Natarajan, S., S. Bordas and D. Roy Mahapatra. Numerical integration over arbitrary polygonal domains based on Schwarz–Christoffel conformal mapping. *International Journal for Numerical Methods in Engineering* 2009; **80(1)**: 103-134.

[36] Natarajan, S., D.R. Mahapatra and S.P.A. Bordas. Integrating strong and weak discontinuities without integration subcells and example applications in an XFEM/GFEM framework. *International Journal for Numerical Methods in Engineering* 2010; **83(3)**: 269-294.

[37] Gross, S. and A. Reusken. An extended pressure finite element space for two-phase incompressible flows with surface tension. *Journal of Computational Physics* 2007; **224(1)**: 40-58.

[38] Béchet, E., H. Minnebo, N. Moës and B. Burgardt. Improved implementation and robustness study of the X-FEM for stress analysis around cracks. *International Journal for Numerical Methods in Engineering* 2005; **64(8)**: 1033-1056.

[39] Babuška, I. and U. Banerjee. Stable Generalized Finite Element Method (SGFEM). *Computer Methods in Applied Mechanics and Engineering* 2012; **201–204(0)**: 91-111.

[40] Sauerland, H. and T.-P. Fries. The stable XFEM for two-phase flows. *Computers & Fluids* 2012**(0)**.

[41] Bathe, K.-J. and E.N. Dvorkin. A four-node plate bending element based on Mindlin/Reissner plate theory and a mixed interpolation. *International Journal for Numerical Methods in Engineering* 1985; **21(2)**: 367-383.

[42] Bletzinger, K.-U., M. Bischoff and E. Ramm. A unified approach for shear-locking-free triangular and rectangular shell finite elements. *Computers & Structures* 2000; **75(3)**: 321-334.

[43] Nguyen-Xuan, H., T. Rabczuk, S. Bordas and J.F. Debongnie. A smoothed finite element method for plate analysis. *Computer Methods in Applied Mechanics and Engineering* 2008; **197(13–16)**: 1184-1203.

[44] Nguyen-Xuan, H., G.R. Liu, C. Thai-Hoang and T. Nguyen-Thoi. An edge-based smoothed finite element method (ES-FEM) with stabilized discrete shear gap technique for analysis of Reissner–Mindlin plates. *Computer Methods in Applied Mechanics and Engineering* 2010; **199(9–12)**: 471-489.

[45] Nguyen-Xuan, H., L.V. Tran, T. Nguyen-Thoi and H.C. Vu-Do. Analysis of functionally graded plates using an edge-based smoothed finite element method. *Composite Structures* 2011; **93(11)**: 3019-3039.

[46] Nguyen-Xuan, H., T. Rabczuk, N. Nguyen-Thanh, T. Nguyen-Thoi and S. Bordas. A node-based smoothed finite element method with stabilized discrete shear gap technique for analysis of Reissner-Mindlin plates. *Computational Mechanics* 2010; **46(5)**: 679-701.

[47] Nguyen-Xuan, H., L.V. Tran, C.H. Thai and T. Nguyen-Thoi. Analysis of functionally graded plates by an efficient finite element method with node-based strain smoothing. *Thin-Walled Structures* 2012; **54**: 1-18.

[48] Nguyen-Thanh, N., T. Rabczuk, H. Nguyen-Xuan and S.P.A. Bordas. A smoothed finite element method for shell analysis. *Computer Methods in Applied Mechanics and Engineering* 2008; **198(2)**: 165-177.

[49] Xu, J., C.K. Lee and K.H. Tan. An XFEM plate element for high gradient zones resulted from yield lines. *International Journal for Numerical Methods in Engineering* 2013; **93(12)**: 1314-1344.

[50] Fries, T.-P. A corrected XFEM approximation without problems in blending elements. *International Journal for Numerical Methods in Engineering* 2008; **75(5)**: 503-532.

[51] Crisfield, M.A. *Non-Linear Finite Element Analysis of Solids and Structures, Volume 2, Advanced topics*. 1 ed John Wiley & Sons: Chichester, 1991.

[52] Zienkiewicz, O.C. and R.L. Taylor. *Finite Element Method (5th Edition) Volume 2 - Solid Mechanics*, 2000, Elsevier.

[53] Abbas, S., A. Alizada and T.P. Fries. The XFEM for high-gradient solutions in convection-dominated problems. *International Journal for Numerical Methods in Engineering* 2010; **82(8)**: 1044-1072.
[54] Owen DRJ, H.E. *Finite element in plasticity, theory and practice*. 1 ed Pineridge Press, Swansea, 1980.
[55] Crisfield, M.A. *Non-Linear Finite Element Analysis of Solids and Structures, Volume 1, Essentials*. 1 ed John Wiley & Sons: Chichester, 1991.
[56] Simo, J.C. and T.J.R. Hughes. *Computational Inelasticity* Springer: New York, 1998.
[57] Olaf Schenk and K. Gaertner. *PARDISO User Guide Version 4.1.2*, 2011.
[58] Johansen, K.W. *Yield-line formulae for slabs* Taylor & Francis, 1972.
[59] Bathe, K.-J. *Finite Element Procedures*. 2 ed Prentice Hall: New Jersey, 1995.
[60] ANSYS Inc. *ANSYS 11.0 Manual*, 2009.

Table 1 The five cases of Example 1

	thickness t	yield strength σ_y	reference loading q_0	thickness/length ratio t / L
T1	0.5	0.4	6.4×10^{-2}	1 / 10
T2	0.25	0.2	8×10^{-3}	1 / 20
T3	0.125	0.1	1×10^{-3}	1 / 40
T4	0.05	0.04	6.4×10^{-5}	1 / 100
T5	0.01	0.008	5.12×10^{-7}	1 / 500

Table 2 Comparison of the computational cost and the condition number of stiffness matrix (Example 1)

	9-node element			6-node element		
	XFEM	FEM (coarse)	FEM (fine)	XFEM	FEM (coarse)	FEM (fine)
n_{DOF}	180	33	2121	180	33	2121
n_{GP}	2700	450	45000	5160	300	30000
n_s	764	787	741	742	735	798
t (second)	1291	83	9113	1173	50	7063
k	6.59E+06	3.56E+03	-	9.82E+05	4.79E+03	-

Table 3 The four cases of Example 2

	thickness t	yield strength σ_y	reference loading q_0
T1	0.15	1	-3.00×10^{-3}
T2	0.1	6.67×10^{-1}	-8.89×10^{-4}
T3	0.03	0.2	-2.40×10^{-5}
T4	0.01	6.67×10^{-2}	-8.89×10^{-7}

Table 4 Comparison of the computational cost and the condition number of stiffness matrix (Example 2)

	9-node element			6-node element		
	XFEM	FEM (coarse)	FEM (fine)	XFEM	FEM (coarse)	FEM (fine)
n_{DOF}	180	33	2121	180	33	2121
n_{Gauss}	2700	450	45000	5160	300	30000
n_s	280	265	292	282	269	286
t (second)	1110.8	27.1	3015.5	512	17.3	1965.2
k	4.37E+10	9.18E+04	-	4.77E+07	1.28E+05	-

Table 5 The four cases of Example 3

	thickness t	yield strength σ_y	reference loading q_0	thickness/length ratio t/L
T1	2.00	2.00×10^5	8.00×10^4	1/16
T2	1.00	1.00×10^5	1.00×10^4	1/32
T3	0.50	5.00×10^4	1.25×10^3	1/64
T4	0.25	2.50×10^4	156.25	1/128

Table 6 Comparison of the computational cost and the condition number of stiffness matrix (Example 3)

	9-node element			6-node element		
	XFEM	FEM (coarse)	FEM (fine)	XFEM	FEM (coarse)	FEM (fine)
n_{DOF}	150	75	5043	132	75	5043
n_{Gauss}	5040	360	36000	4380	240	24000
n_s	108	104	116	120	109	114
t (second)	164.3	7.9	853.5	142.4	5.3	568.2
k	1.03E+10	6.12E+03	-	4.13E+05	5.07E+04	-

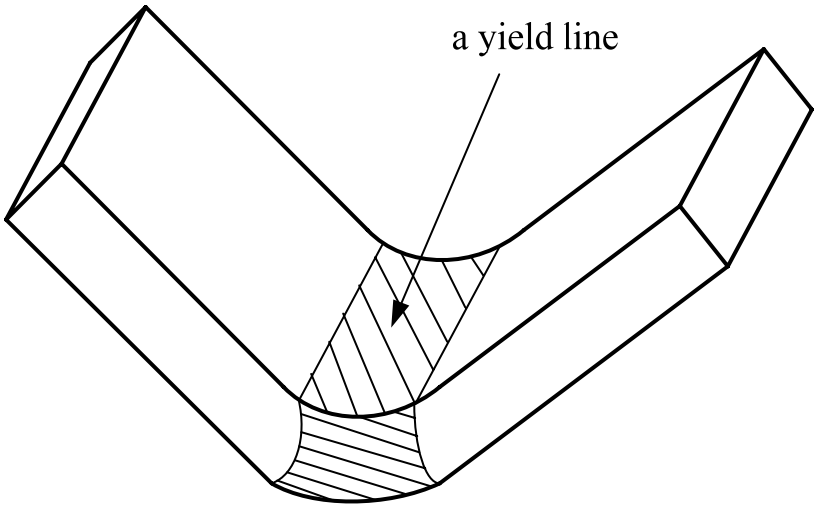

Figure 1 A yield line in a plate structure

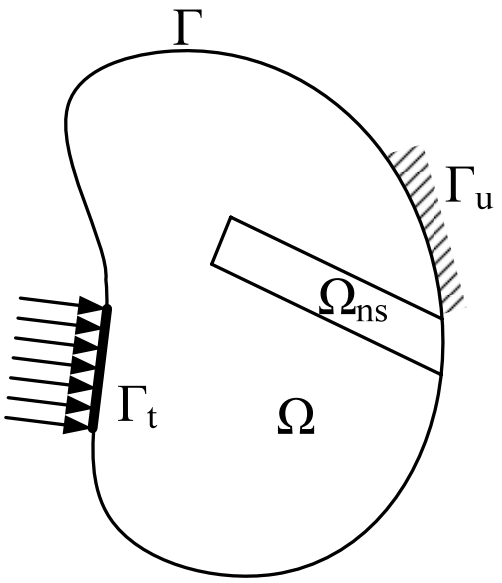

Figure 2 A domain with a high gradient zone inside

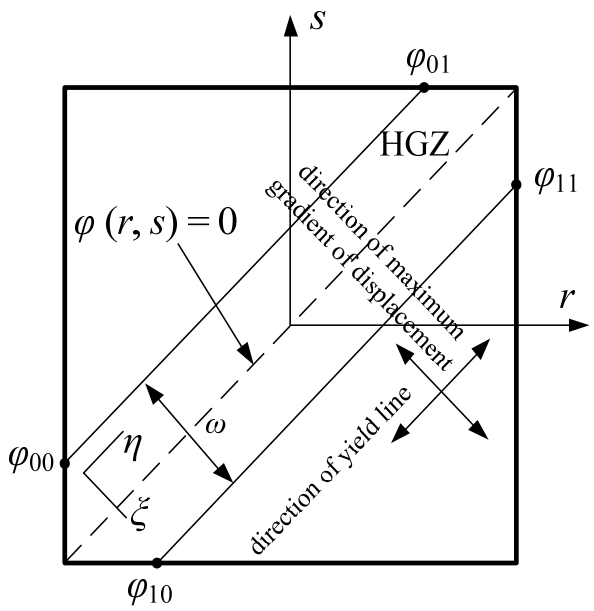

Figure 3 A quadrilateral element with a high gradient zone

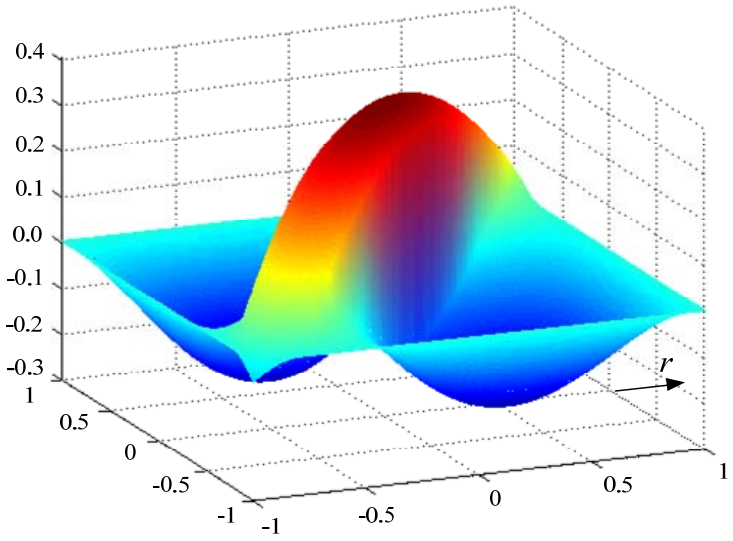

(a) The 3D plot of F in a 9-node quadrilateral element

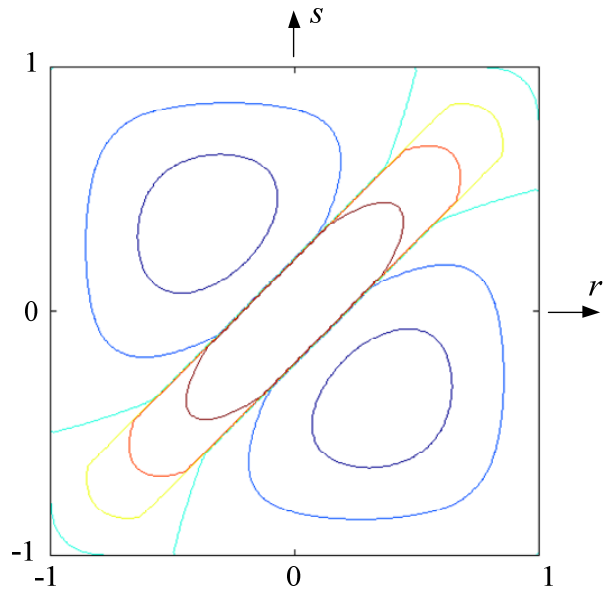

(b) The contour of F in a 9-node quadrilateral element

Figure 4 The plot of F in a 9-node quadrilateral element

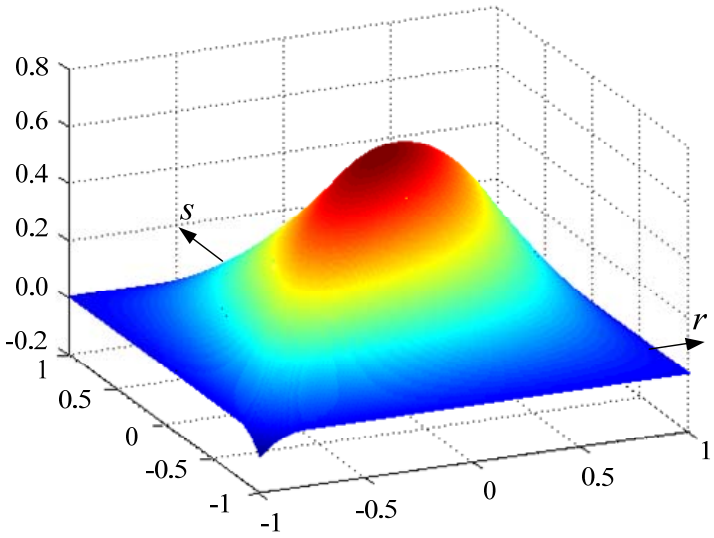

(a) The 3D plot of the modified F in a 9-node quadrilateral element

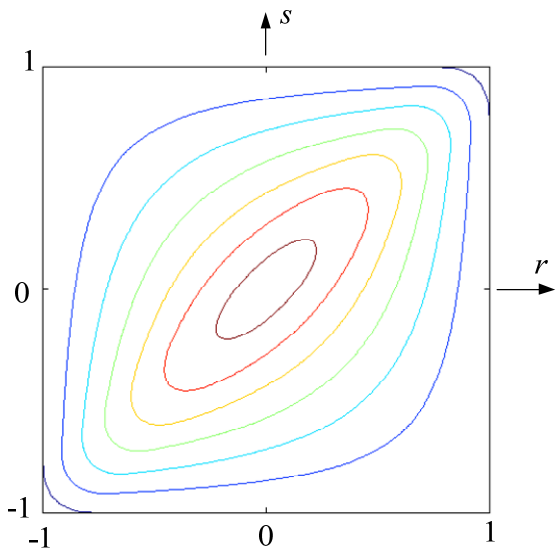

(b) The contour of the modified F in a 9-node quadrilateral element

Figure 5 The plot of the modified F in a 9-node quadrilateral element

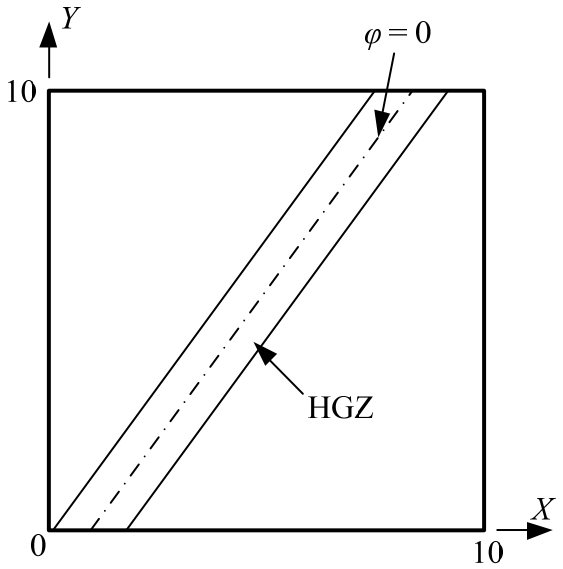

Figure 6 An example of HGZ

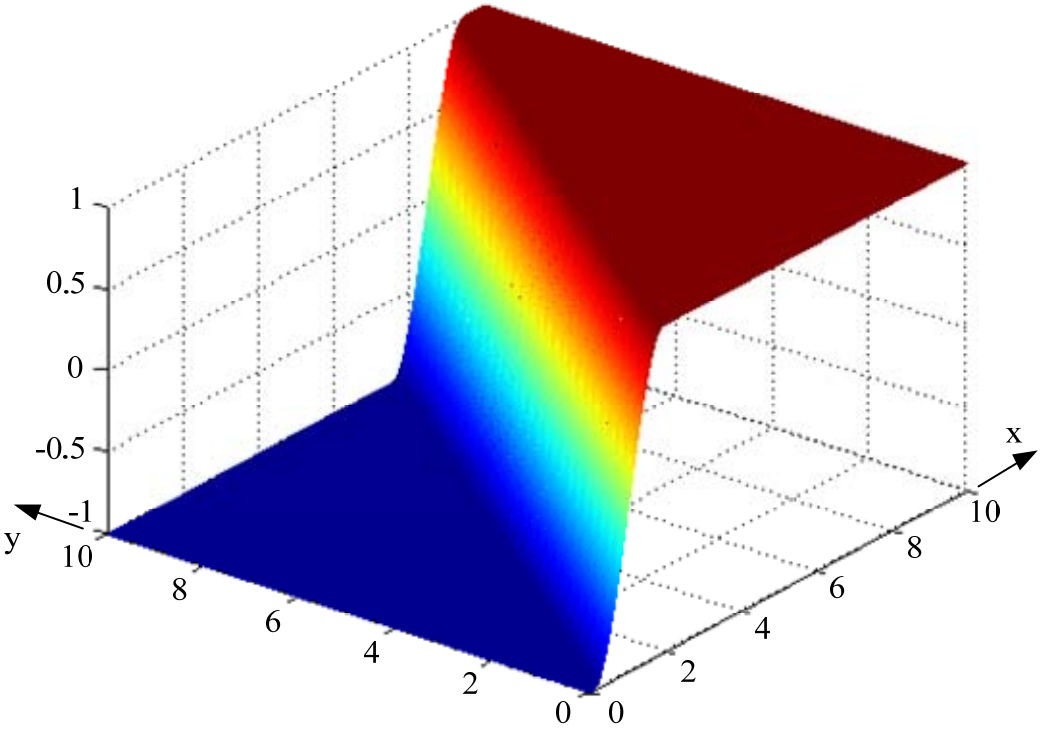

Figure 7a The 3D plot of *R*

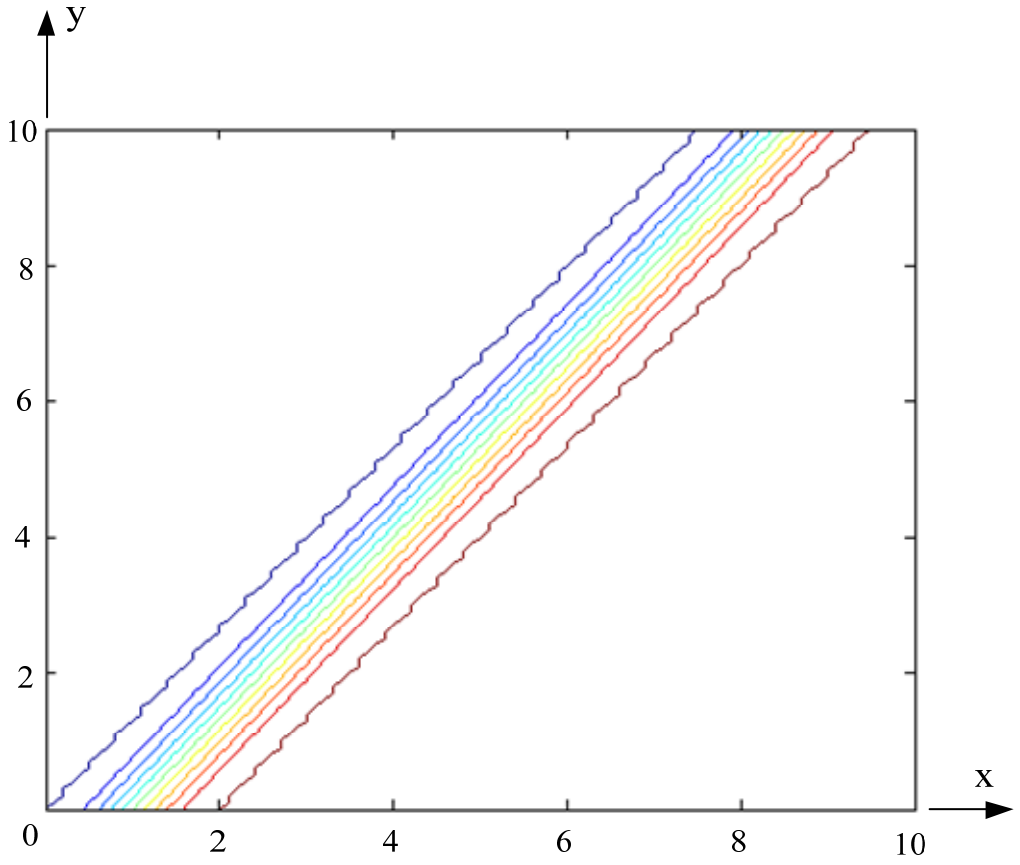

Figure 7b The contour of *R*

Figure 7 The plot of R

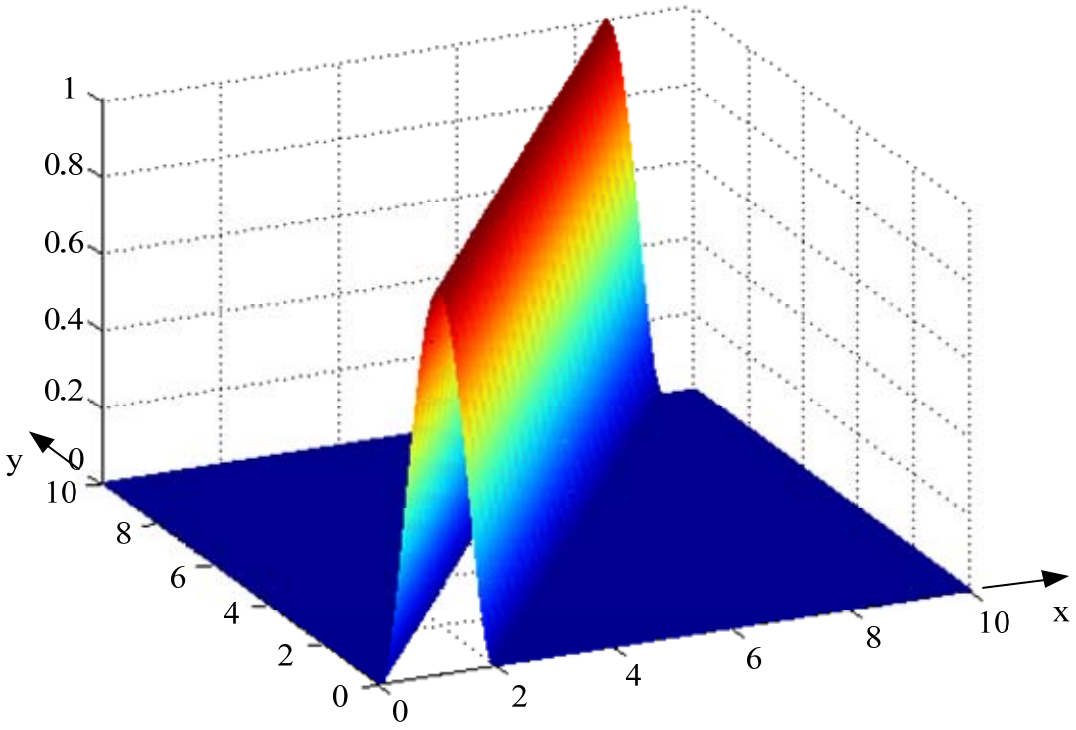

Figure 8a The 3D plot of F

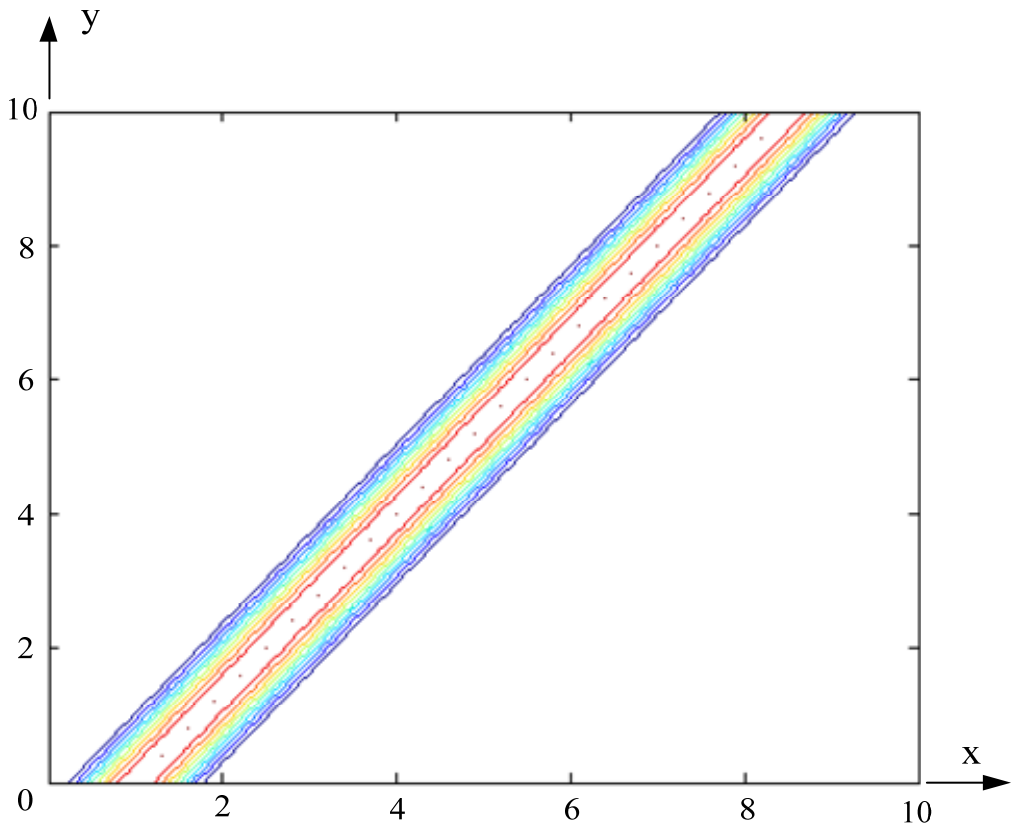

Figure 8b The contour of F

Figure 8 The plot of F

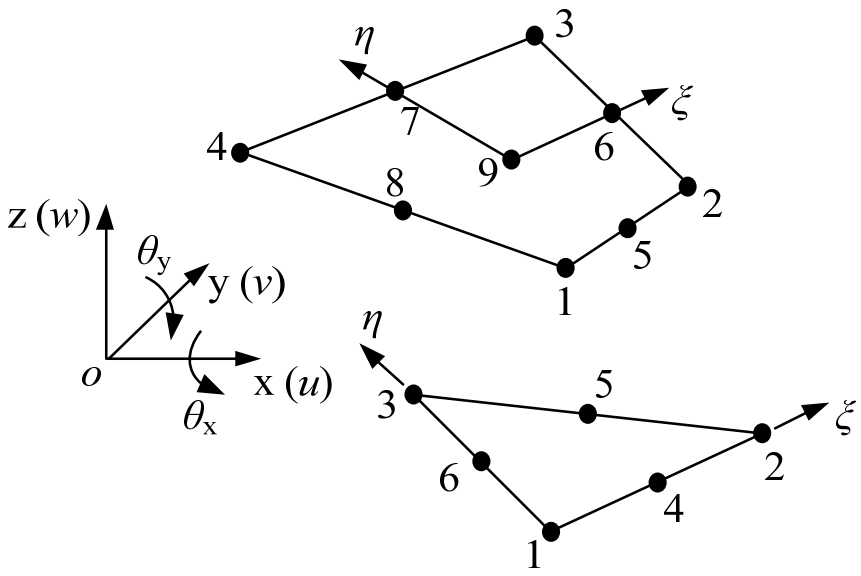

Figure 9 The coordinate system for the plate elements

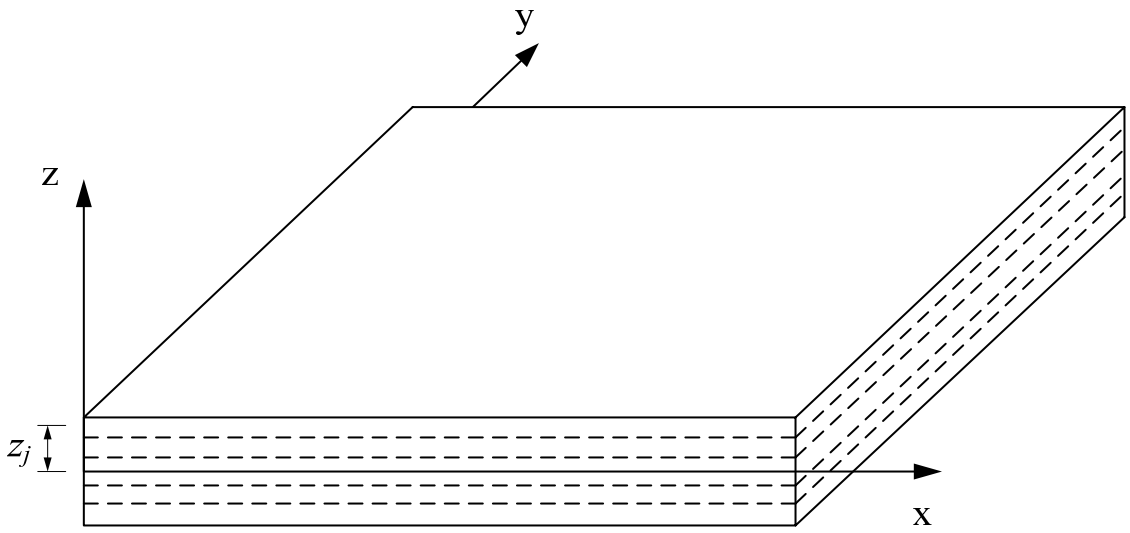

Figure 10 The layered model

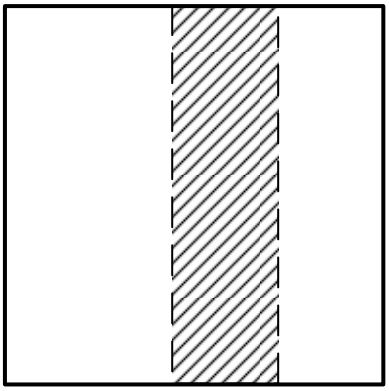

Figure 11a 2 QU_nH + 1 QU_H

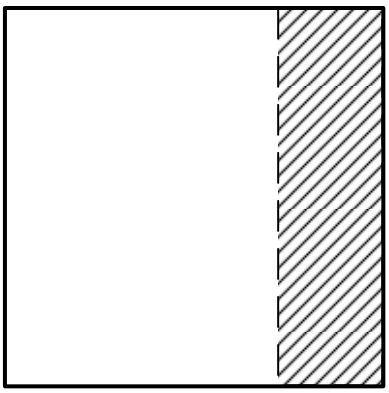

Figure 11b 1 QU_nH + 1 QU_H

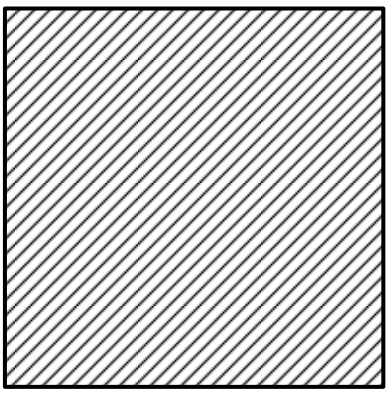

Figure 11c 1 QU_H

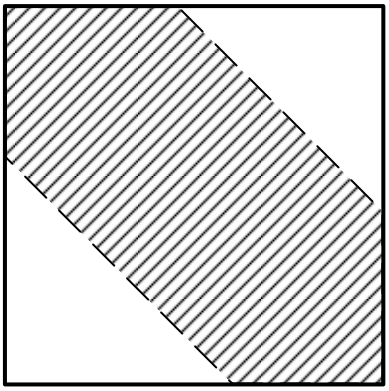

Figure 11d 2 TR_nH + 1 HE_H

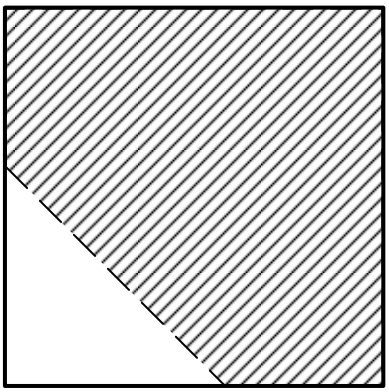

Figure 11e 1 TR_ nH + 1 PE_H

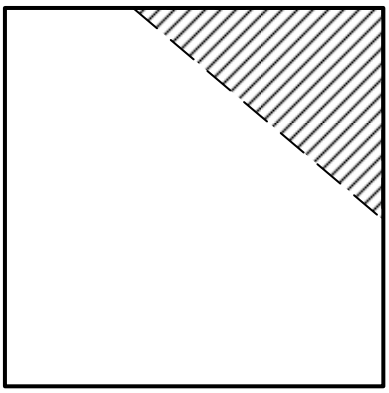

Figure 11f 1 PE_nH + 1 TR_H

Figure 11 Partition of a 9-node XFEM element

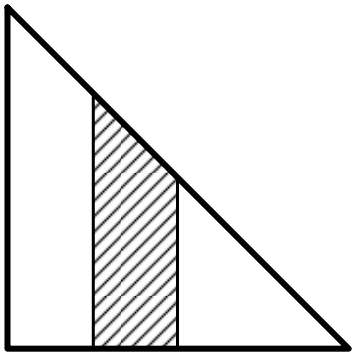

Figure 12a 1 TR_nH + 1 QU_nH + 1 QU_H

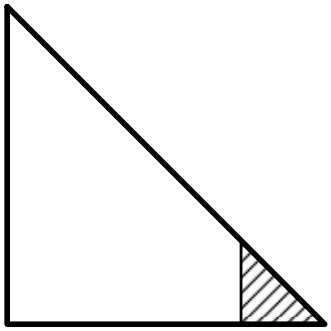

Figure 12b 1 QU_nH + 1 TR_H

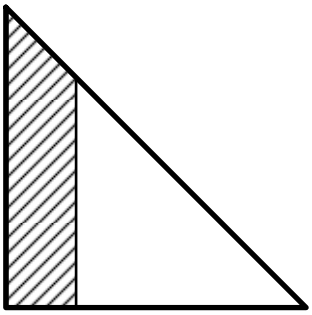

Figure 12c 1 TR_nH + 1 QU_H

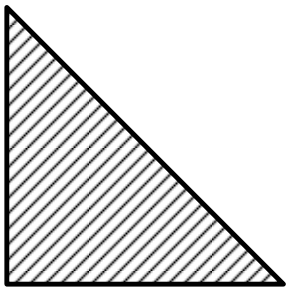

Figure 12d 1 TR_H

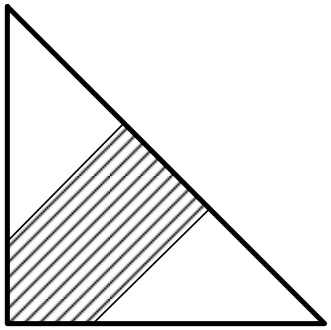

Figure 12e 2 TR_nH + 1 PE_H

Figure 12 Partition of a 6-node XFEM element

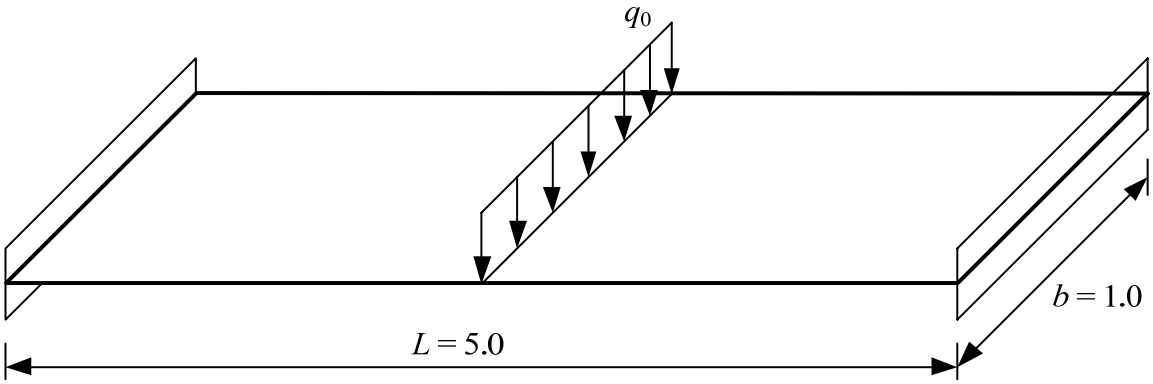

Figure 13 Example 1: the flat strip with two fully fixed ends

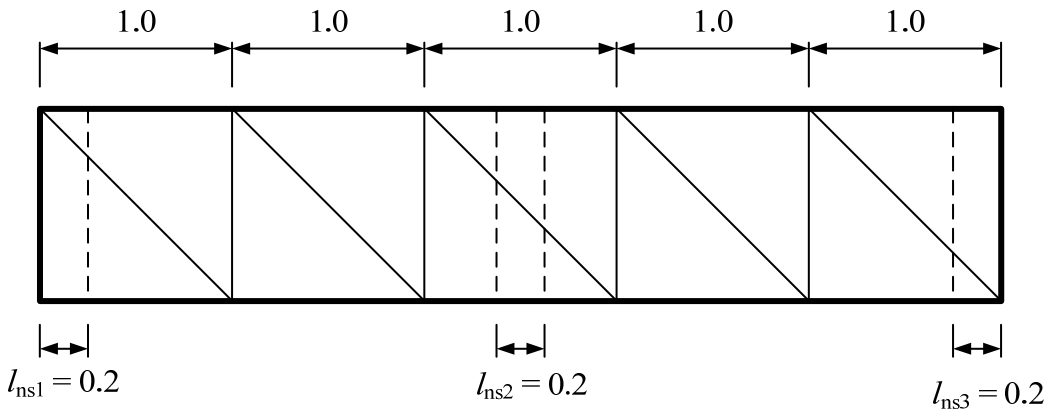

Figure 14a the uniform mesh with 6-node elements

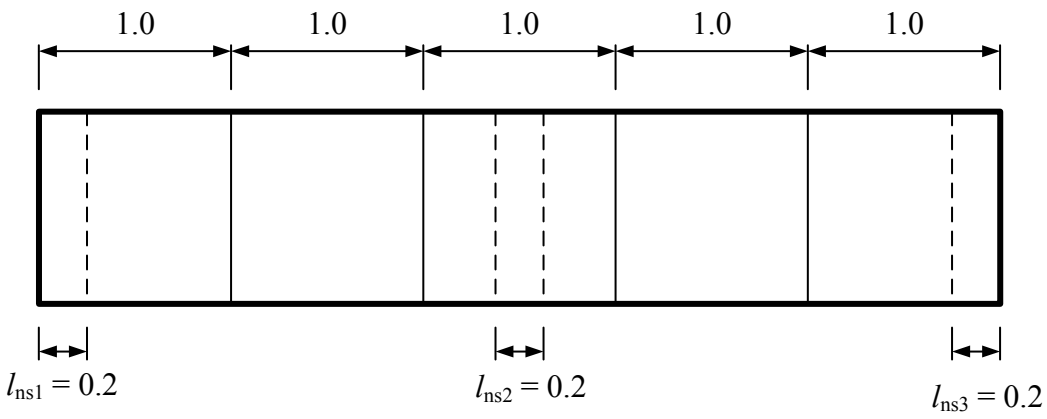

Figure 14b the uniform mesh with 9-node elements

Figure 14 the uniform mesh of Example 1

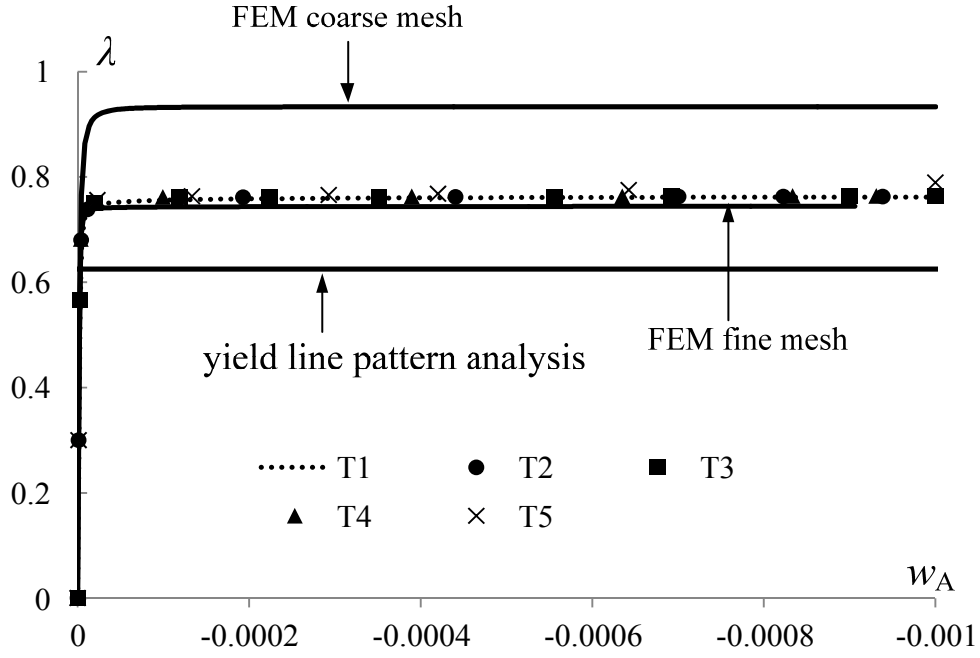

Figure 15 The equilibrium path of Example 1 by 6-node elements

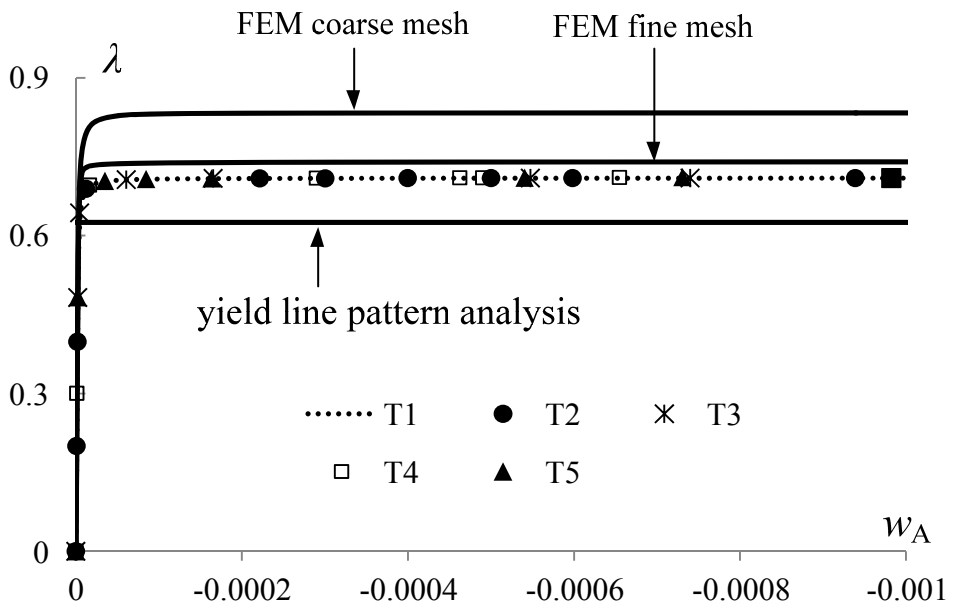

Figure 16 The equilibrium path of Example 1 by 9-node elements

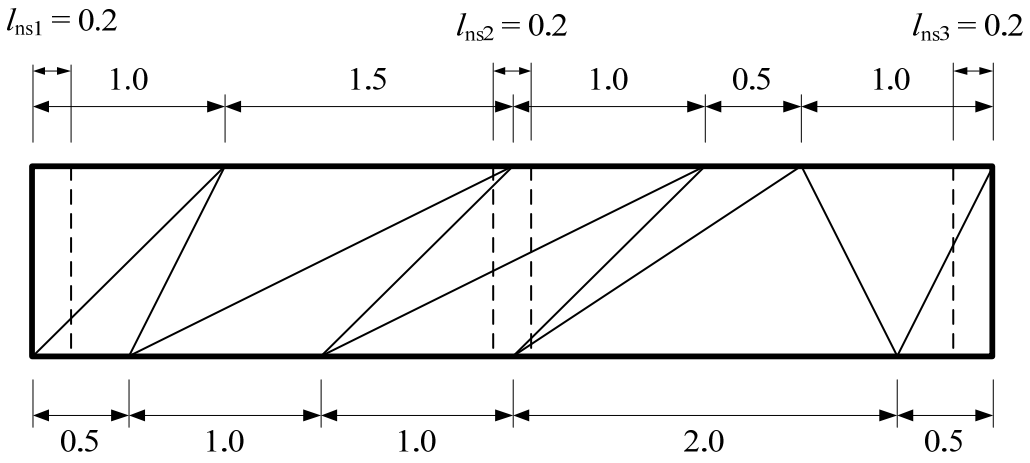

Figure 17a The distorted mesh with 6-node elements

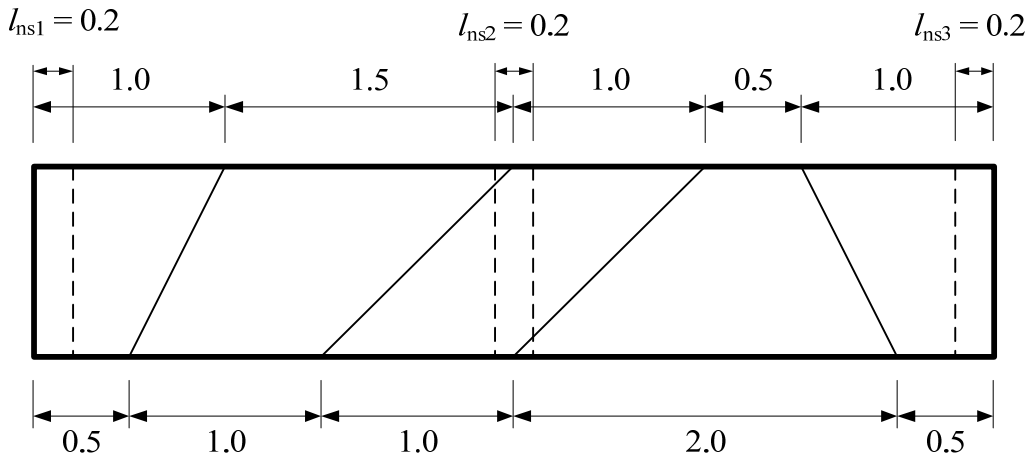

Figure 17b The distorted mesh with 9-node elements

Figure 17 The distorted mesh of Example 1

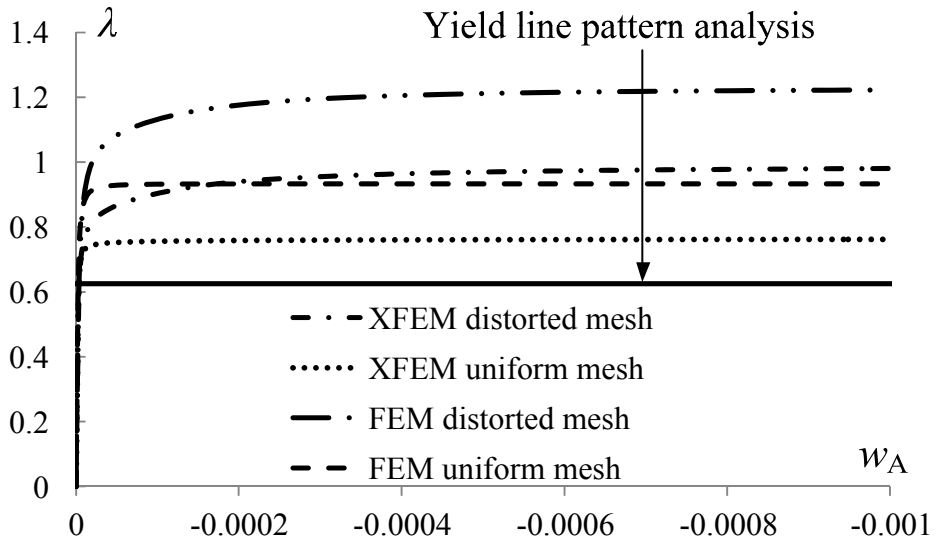

Figure 18 The equilibrium path of Example 1 by 6-node elements distorted mesh

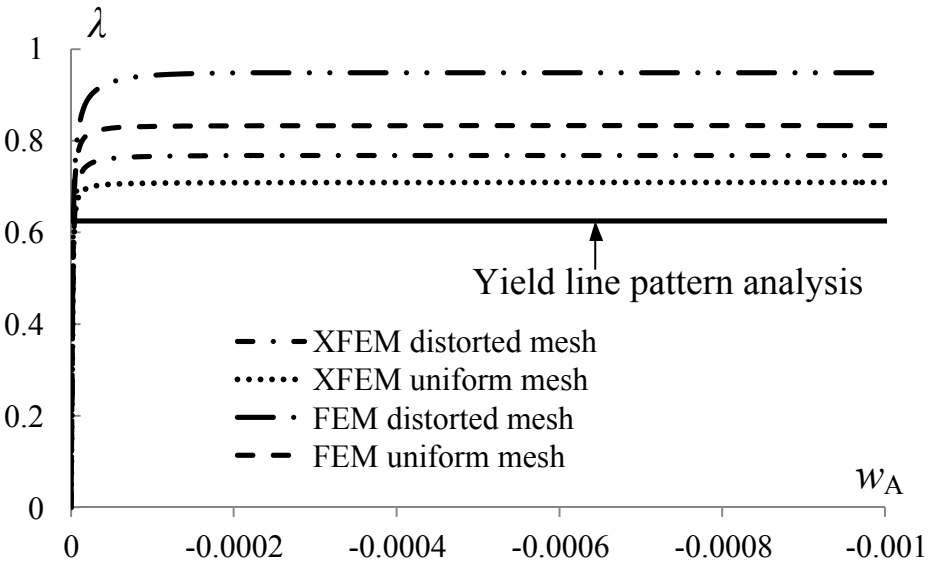

Figure 19 The equilibrium path of Example 1 by 9-node elements distorted mesh

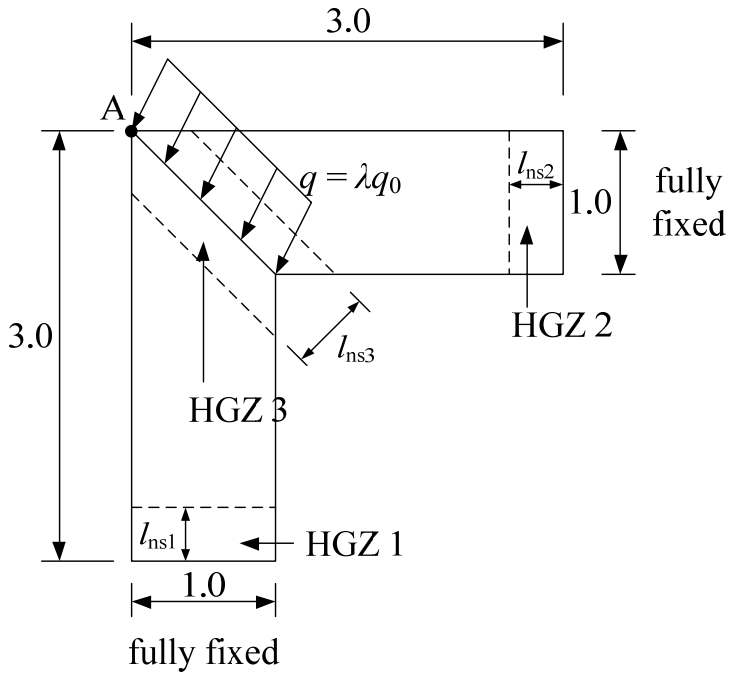

Figure 20 Example 2: the L-shape plate

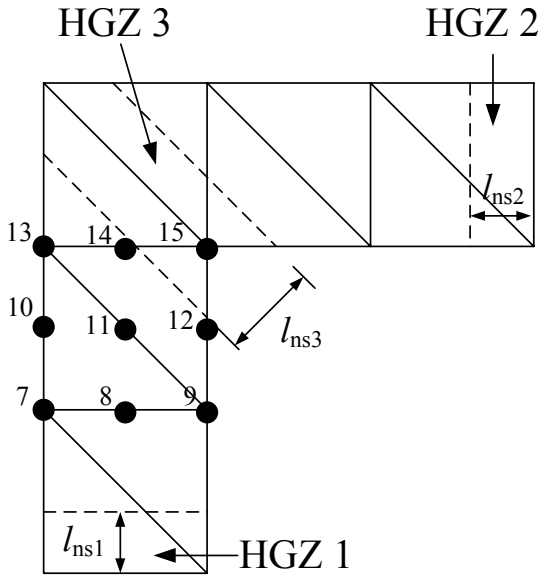

Figure 21a The mesh for the 6-node XFEM element

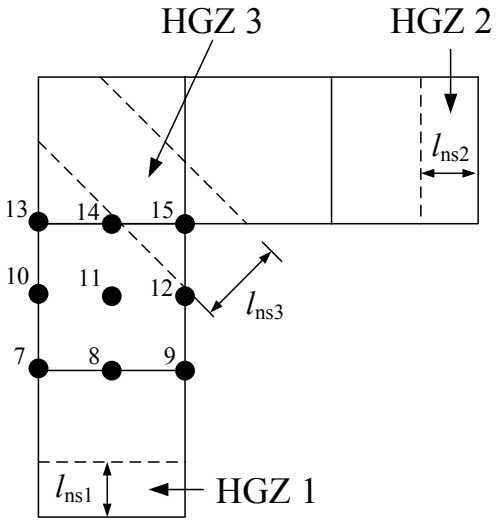

Figure 21b The mesh for the 9-node XFEM element

Figure 21 The mesh pattern of the L-shape plate

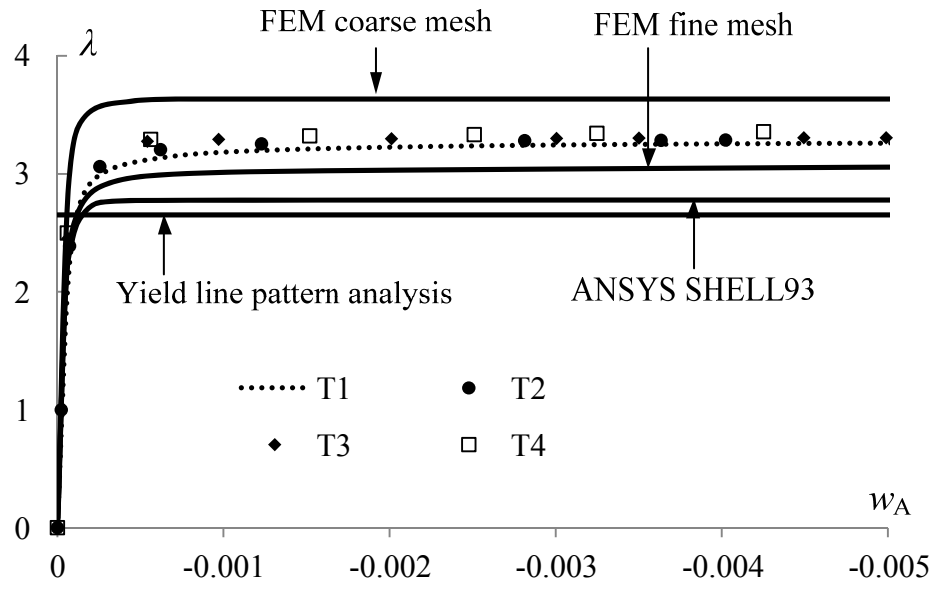

Figure 22 The equilibrium path of Example 2 by 6-node elements

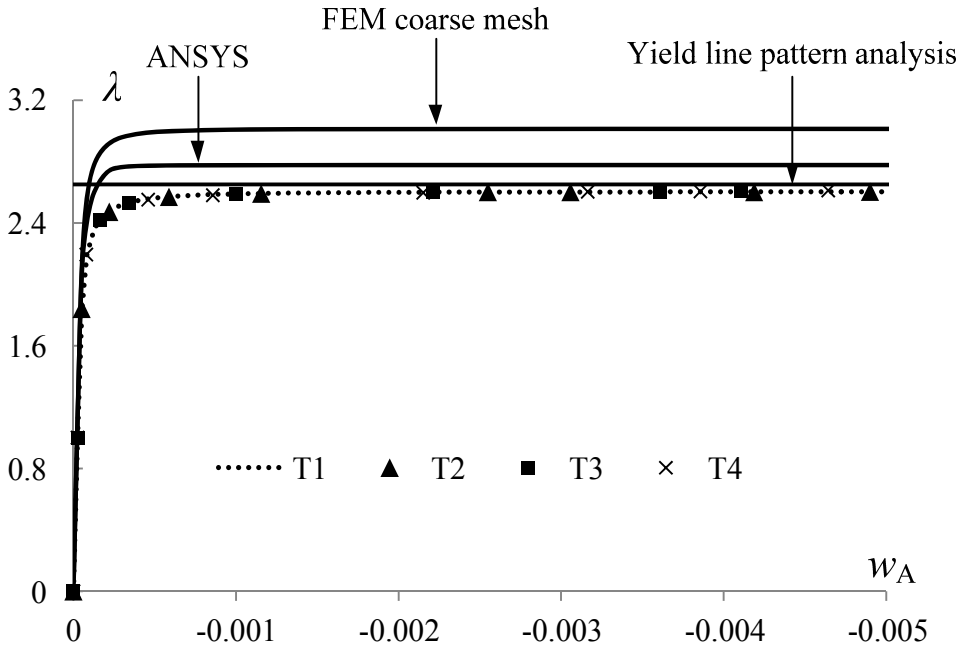

Figure 23 The equilibrium path of Example 2 by 9-node elements

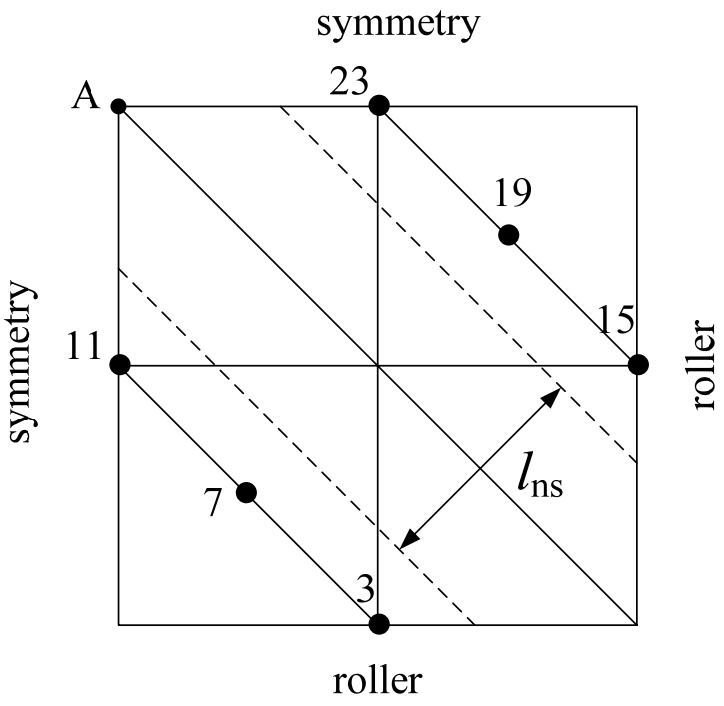

Figure 24a The mesh pattern for 6-node elements (mesh pattern 1)

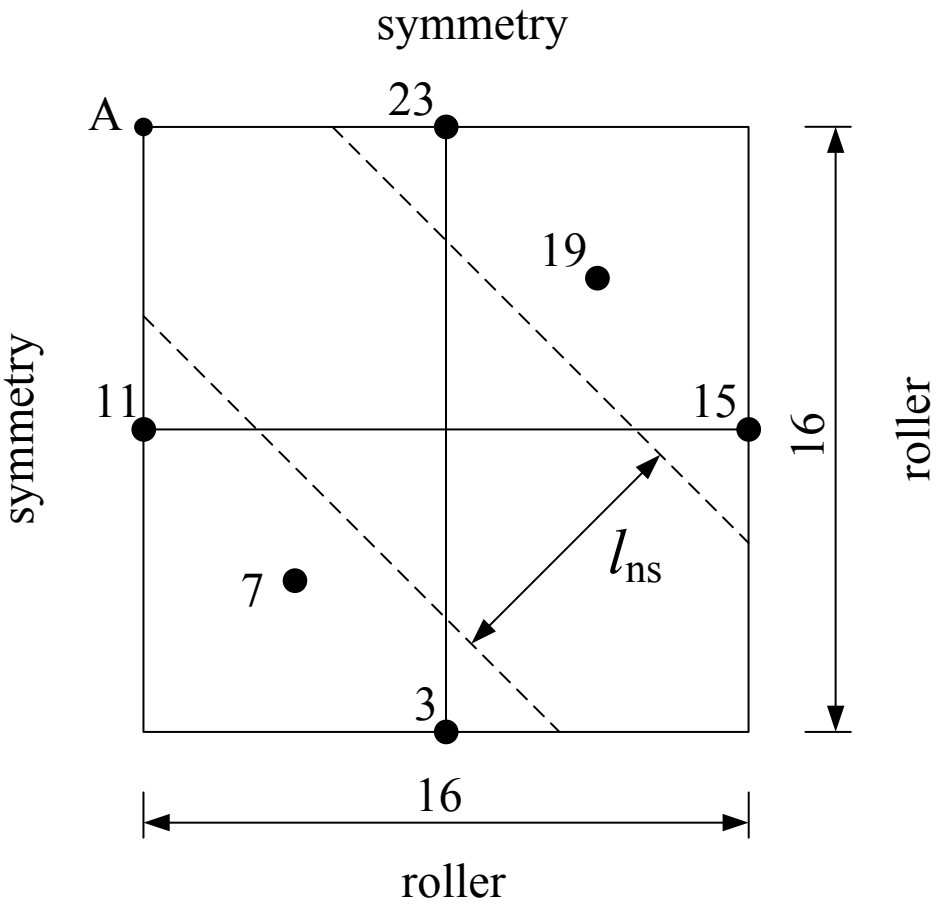

Figure 24b The mesh pattern for 9-node elements

Figure 24 Example 3: the square plate with roller support on four edges

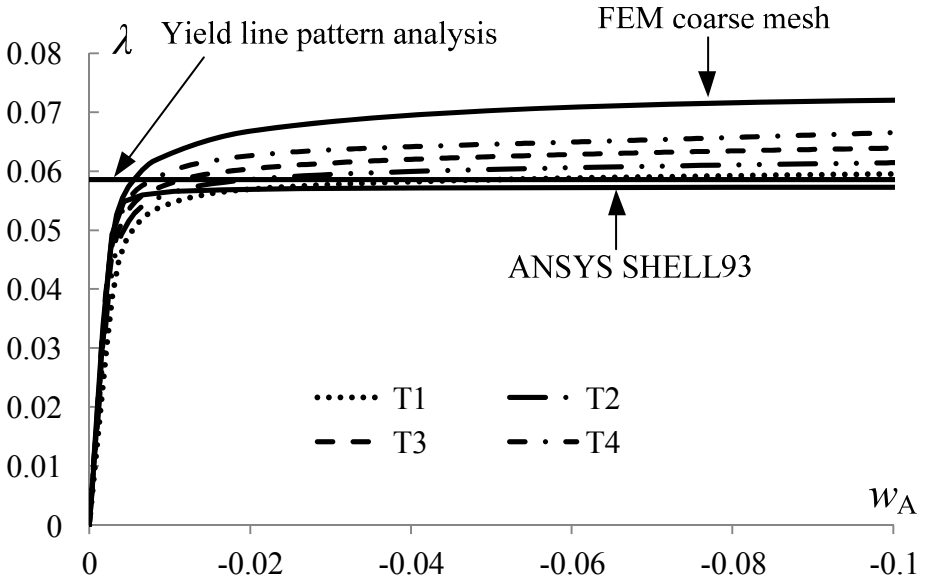

Figure 25 The equilibrium path of Example 3 by 6-node elements

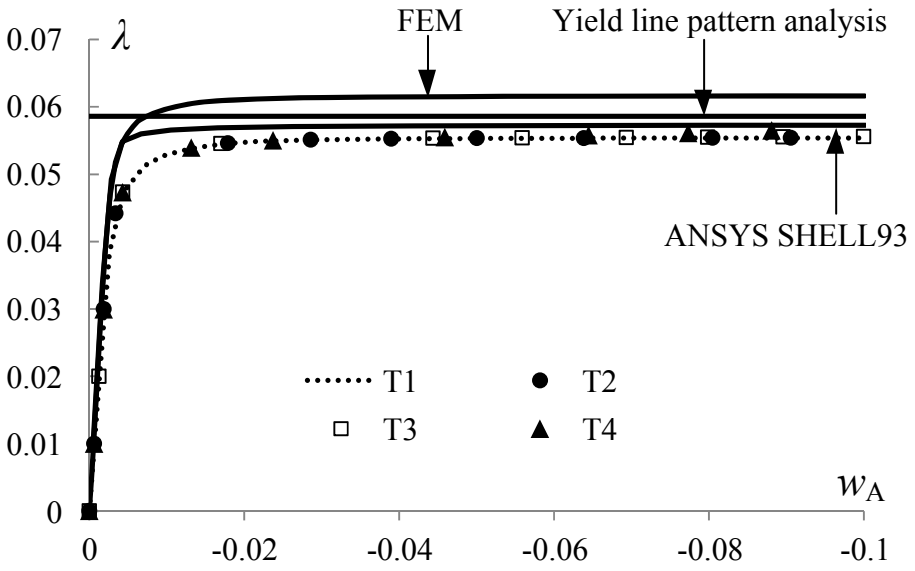

Figure 26 The equilibrium path of Example 3 by 9-node elements

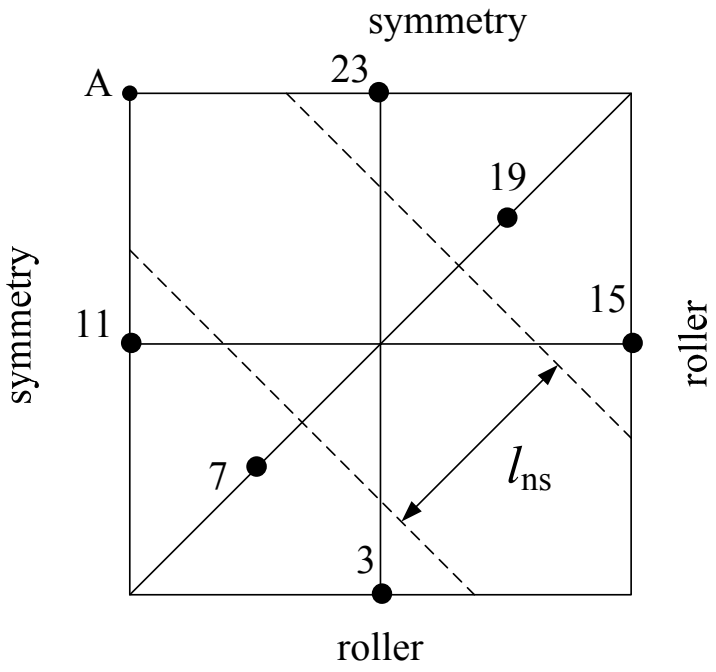

Figure 27 The alternative mesh scheme for the 6-node XFEM formulation (mesh pattern 2)

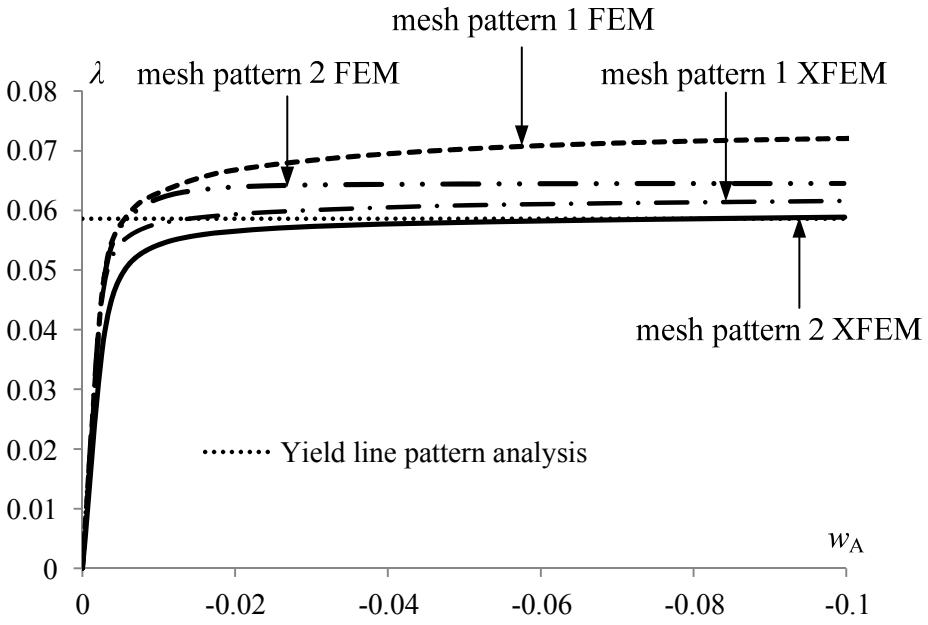

Figure 28 The equilibrium path of Example 3 by 6-node XFEM formulation with different mesh scheme